May 2018

Depositionally-Induced Magnetic Frequency Variations of a Sandstone Facies of the Copper Harbor Conglomerate from the North American, Mid-Continent Rift at Union Bay, Michigan

Elizabeth Anne Borucki
University of Wisconsin-Milwaukee

Recommended Citation

Borucki, Elizabeth Anne, "Depositionally-Induced Magnetic Frequency Variations of a Sandstone Facies of the Copper Harbor Conglomerate from the North American, Mid-Continent Rift at Union Bay, Michigan" (2018). *Theses and Dissertations*. 1758.
https://dc.uwm.edu/etd/1758

DEPOSITIONALLY-INDUCED MAGNETIC FREQUENCY VARIATIONS OF A SANDSTONE FACIES OF THE COPPER HARBOR CONGLOMERATE FROM THE NORTH AMERICAN, MID-CONTINENT RIFT AT UNION BAY, MICHIGAN

by

Elizabeth Anne Borucki

A Thesis Submitted in
Partial Fulfillment of the
Requirements for the Degree of

Master of Science
in Geosciences

at
The University of Wisconsin-Milwaukee
May 2018

ABSTRACT

DEPOSITIONALLY-INDUCED MAGNETIC FREQUENCY VARIATIONS OF A SANDSTONE FACIES OF THE COPPER HARBOR CONGLOMERATE FROM THE NORTH AMERICAN, MID-CONTINENT RIFT AT UNION BAY, MICHIGAN

by

Elizabeth Anne Borucki

The University of Wisconsin-Milwaukee, 2018
Under the Supervision of Professor Dr. Julie Bowles

The Mesoproterozoic, Copper Harbor Conglomerate Sandstone Facies of Union Bay, Michigan was investigated to determine whether fluvial red beds from deep time can maintain magnetic variations related to deposition. Additionally, the possibility that magnetic variations represent astronomically forced climate cycles was also explored at this site. The study utilized environmental magnetism and cyclostratigraphic techniques. The magnetic mineralogy was characterized using temperature dependent susceptibility, isothermal remanent magnetization, and anisotropy of magnetic susceptibility to determine composition, approximate grain size, abundance, and magnetic shape and orientation. For a partial cyclostratigraphic study, sequential, outcrop based magnetic susceptibly measurements were taken stratigraphically every 0.47 m on average, over 56.4 m. Fine-grained magnetite and hematite were inferred from laboratory measurements, and the assemblage of magnetic grains were determined to be primarily prolate. The magnetic fabric agreed with previous paleocurrent field observations at the site, with a flow directionality towards the northwest, suggestive that susceptibility correlates with depositional orientation. Hematite concentration was determined to control susceptibility, and fluctuations in its abundance were observed to be related to physical outcrop properties.

High susceptibility corresponded with physically larger grain sizes and was associated with cross-bedding, meanwhile low susceptibility was attributed to physically smaller grain sizes as well as erosional and color boundaries. A statistically-significant periodic susceptibility signal was observed approximately every 2 m from the stratigraphy. The cyclicity of the signal suggests that susceptibility variations may arise from climatically-induced variations in depositional or post-depositional processes. Due to the uncertainty in the positioning of this section in absolute time, our study precludes a relationship between the observed periodic signal and astronomically forced climate cycles. However, the ability to isolate a cyclical signal in these deep time, fluvial red beds suggest that Precambrian deposits are potential candidates for full cyclostratigraphic studies provided there are fewer unknowns related to absolute depositional timescales.

TABLE OF CONTENTS

LIST OF FIGURES

LIST OF TABLES

LIST OF ABBREVIATIONS

χ	volume normalized magnetic susceptibility [SI]
$\chi(T)$	magnetic susceptibility as a function of temperature [SI]
χ_B	mass normalized bulk susceptibility [m^3/kg]
τ_1	maximum eigenvalue
τ_2	intermediate eigenvalue
τ_3	minimum eigenvalue
AF	alternating field
AMS	anisotropy of magnetic susceptibility
ARM	anhysteretic remanent magnetization
B_h	peak coercivity of skew-normal distribution derived from IRM un-mixing
bya	billion years ago
CHC	Copper Harbor Conglomerate
DP	dispersion parameter
EC	extrapolated contribution
F	foliation parameter (τ_2/τ_3)
Ga	billion years
Hard-IRM	high coercivity isothermal remanent magnetization
IRM	isothermal remanent magnetization
IRM_{1T}	isothermal remanent magnetization acquired in 1 T forward field
IRM_{-300mT}	isothermal remanent magnetization acquired in 300 mT back field
kyr	kiloyear (thousand years)

L	lineation parameter (τ_1/τ_2)
MCR	mid-continent rift
MD	multi-domain
MISS	microbial influenced sedimentary structure
MTM	multi-taper method
NRM	natural remanent magnetization
OC	observed contribution
P	anisotropy degree (τ_1/τ_3)
PSD	pseudo-single-domain
S-ratio	saturation ratio
SD	single-domain
SIRM	saturation isothermal remanent magnetization
Soft-IRM	low coercivity isothermal remanent magnetization
SP	superparamagnetic
T_C	Curie temperature [ºC]
V_1	maximum eigenvector
V_2	intermediate eigenvector
V_3	minimum eigenvector

ACKNOWLEDGMENTS

First and foremost, I would like to thank my advisor Dr. Julie Bowles of the Department of Geosciences at the University of Wisconsin-Milwaukee. Julie has been a truly amazing advisor and is sincerely a kind and generous person. She willingly agreed to conduct field work in the Upper Peninsula of Michigan at the end of May in torrential downpours and temperatures barely above freezing—all while camping! She also always leaves her office door open for my countless questions about everything. I could not have asked for a better advisor, she goes above and beyond in everything that she does and is always willing to share her time, thoughts, and expertise. I am so fortunate to have worked with such a brilliant person.

I would also like to thank the Department of Natural Resources of the state of Michigan for working with me throughout my sample collection permitting process. The state permitted and allowed for the collection of rock samples from the Porcupine Wilderness State Park of the Upper Peninsula of Michigan, the research presented in this thesis would not have been possible without their authorization. Additionally, I truly appreciate the funding support provided through The University of Wisconsin Milwaukee, The Wisconsin Space Grant Consortium, The Greater Milwaukee Foundation, and The Geological Society of America. Their monetary support ensured funding both in the field and out, they also provided the opportunity to present my research at the annual, national conference of The Geological Society of America in 2017.

To Jenny Ulbricht, my fellow Copper Harbor Conglomerate investigator, thank you for your willingness to talk about depositional conditions or paleocurrent orientations at the drop of a hat! Thank you for taking me up to Union Bay for the first time and letting me explore the site

of my future thesis research even before I began my graduate studies. Most importantly though, CHC forever, or at least a billion years!

To the entire faculty of the Department of Geosciences at the University of Wisconsin-Milwaukee, especially Dr. John Isbell and Dr. Barry Cameron, thank you for seeing my potential as an undergraduate and encouraging me to pursue higher education. Thank you for the countless letters of recommendation and for sitting on my committee. I would also like to thank Dr. Bill Kean for sitting on my committee and offering up so much advice on how to organize my abstract and conclusions. I am so honored to have continued my education with this department from my undergraduate to graduate degree!

Thank you to my fellow graduate students, Megan Barlow, Emily Joynt, Kate Pauls, Nick Fedorchuck, David Cordie, Chase Glenister, Keenan Hassel, Kate Gigstad, Jenny Ulbricht, Andy Wanta, Maddy Salo, and Sheryl Stephenson for filling the past two years with so much laughter, support, encouragement, and enthusiasm. All of you have given so much meaning to this entire experience; the late nights, over-practiced talks, post colloquium Tea Time tradition, and last minute edits will be remembered forever.

Lastly, I would like to thank my parents, David and Karyn Borucki for your constant encouragement and support in everything I have ever done. You never questioned when I left art school to pursue a science degree, you only ever thought I could succeed. Your constant, unwavering belief in me has given me all the confidence I need to know that whatever I put my mind to, I can accomplish. Without either of you, none of this would be possible.

CHAPTER 1. INTRODUCTION

1.1 General Introduction

Magnetic properties of rocks and sediments are used to study a wide variety of geologic processes, such as geomagnetic field variations, tectonic reconstructions, and paleoenvironmental variations (Dekkers, 2001). Magnetostratigraphy is a common application that involves using geomagnetic polarity reversals to constrain absolute timescales in the stratigraphic record. Because polarity reversals happen so infrequently and irregularly (on time scales of tens of thousands to millions of years), temporal resolution is necessarily low. By contrast, environmental magnetism concerns itself with higher frequency variations such as orientation, concentration, and variability of iron-bearing minerals in relation to fluctuations in the depositional record (Liu et al., 2012). Climatically-driven depositional variations in magnetic properties can sometimes be linked to well-recognized orbital frequencies ranging from tens to hundreds of thousands of years. When the cyclic data are combined with the magnetostratigraphy, it may be possible to establish higher resolution timescales within an absolute time interval. The combination of these two areas of study is known as magnetocyclostratigraphy.

For example, a study conducted by Kodama et al. (2010) developed a magnetostratigraphy using thermal demagnetization data that established several absolute time tie points for a section of the Eocene age, Arguis Formation in the Spanish Pyrenees. Stratigraphic variations in the concentration of magnetic minerals was assessed at high resolution using anhysteretic remanent magnetization (ARM) measurements. An initial, un-tuned spectral analysis of the ARM data revealed seven significant peaks at 0.012 m^{-1}, 0.019 m^{-1}, 0.033 m^{-1}, 0.068 m^{-1}, 0.179 m^{-1}, 0.190 m^{-1}, and 0.211 m^{-1} within their measured stratigraphic section (Kodama et al., 2010). It was determined, using the average accumulation rate, that these peaks represented time intervals close to those of orbital variations of short eccentricity (80-125 kyr) and long eccentricity (405 kyr). This spectral data was then fine-tuned and scaled using a variety of filters and models (Kodama et al., 2010). The filters and tuning of the spectral data generated strong peaks for long and short eccentricity (400 kyr, and 95 to 128 kyr) as well as precession (23 kyr, 22 kyr, 19 kyr) (Kodama et al., 2010). The spectral output was then used to refine the absolute timescale in between polarity boundaries (Kodama et al., 2010). The periodic variations in magnetic properties, as determined by Kodama et al. (2010), provided a higher-resolution timescale than magnetostratigraphy alone, providing more detailed insight into past environmental, climatic, or accumulation rate variations.

Cyclostratigraphy is a broad field that aims to collect high-resolution data over sometimes quite long, stratigraphic intervals (Kodama and Hinnov, 2015). In the past, properties such as lithologic or isotope variations have been used to identify cyclic intervals related to astronomically forced climate changes (e.g., Olsen et al., 1996 and Hays et al., 1976). However, data such as that obtained from the collection of magnetic susceptibility measurements are becoming more widely used in this field. This is due to the relatively non-invasive techniques and high-resolution data that can be acquired from measuring magnetic susceptibility at the outcrop. Iron bearing minerals are reflective of environmental and climatic history since they are sensitive to not only the conditions of their original formation, but also changes in depositional history and post-depositional alteration (Liu et al., 2012), all of which may be influenced by climate.

Traditionally, magnetocyclostratigraphy has been tested on marine sediments as they are representative of more continuous deposition. However, Kodama (2016) successfully identified an eccentricity and obliquity signal in the 330 Ma fluvial red beds of the Mauch Chunk formation in Pennsylvania using outcrop based magnetic susceptibility measurements. The Mauch Chunk developed under semi-arid conditions in a sub-aerial to fluvial environment through deltaic progradation (Vrazo et al., 2007). The Mauch Chunk formation shares similarities with the depositional history of the 1.1 Ga Copper Harbor Conglomerate which developed under arid conditions and was deposited through alluvial fan deposition that fed into ephemeral bodies of water (Wolff and Huber, 1973; Elmore, 1984). The goal of this thesis is to determine if it is possible to isolate a cyclic signal linked to climate or deposition in the Precambrian rock record, using magnetic susceptibility. This thesis focuses on a small section of the Porcupine Wilderness State Park, Michigan, that hosts a sandstone facies of the Copper Harbor Conglomerate (CHC) (Fig. 1). The measurements and samples for this research were selected and obtained from a small section of fine- to medium-grained sandstones that featured a variety of sedimentary bed-forms. Physical properties studied included the magnetic mineral abundance, arrangement, composition, and grain size. The characterization of these magnetic properties allowed for the assessment of the degree to which magnetic mineralogy may be linked to depositional variations at this locality.

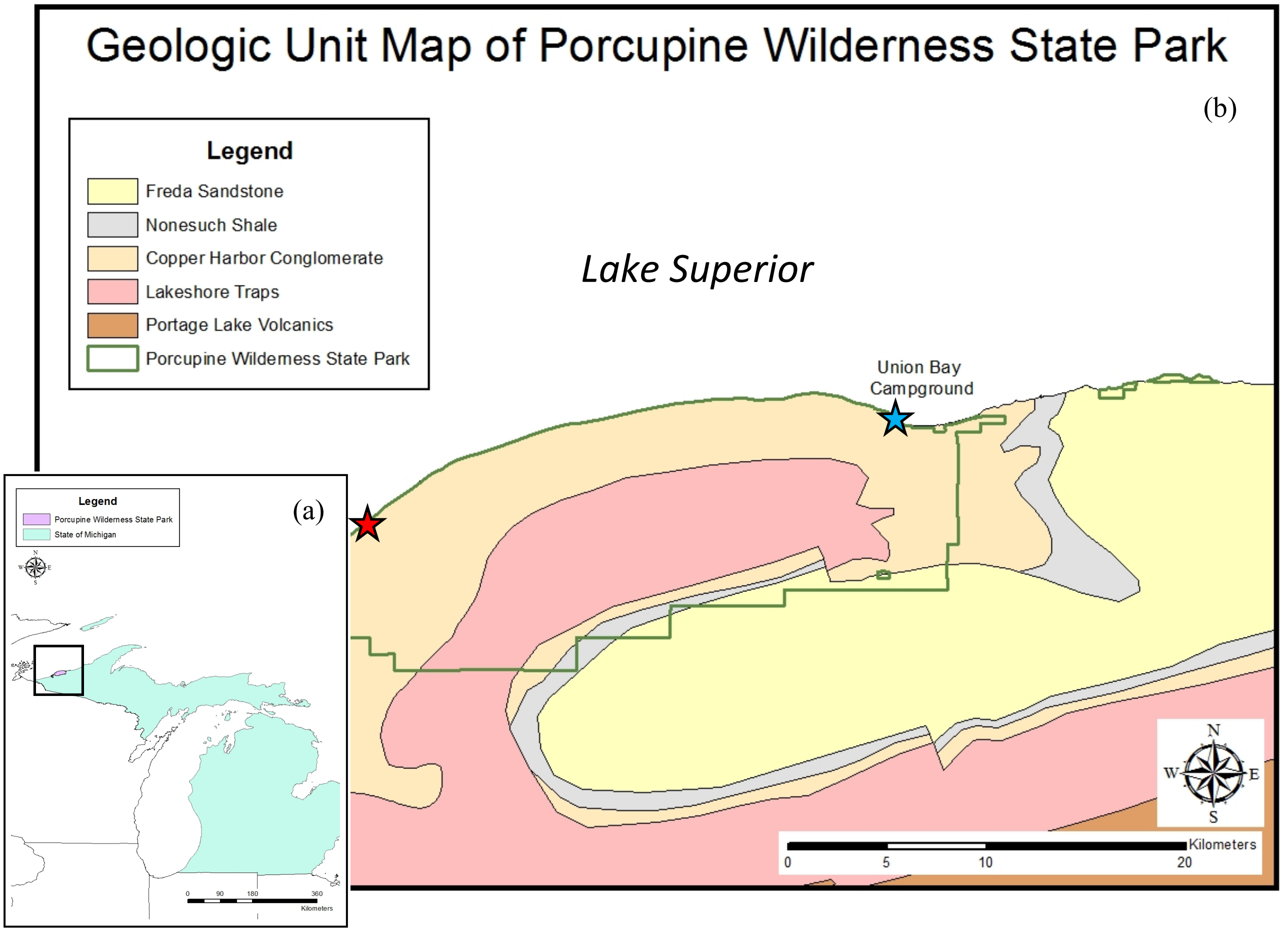

Figure 1: Geologic map of Porcupine State Park

(a) The inset map highlights the study area, particularly the Upper Peninsula of Michigan. The research for this thesis is focused within the Porcupine Wilderness State Park, highlighted in light pink, and enclosed by the black box outline. (b) Field Locality 1 is at Union Bay Campground, highlighted by the blue star. Field Locality 2 is highlighted by the red star. The samples were selected from the Copper Harbor Conglomerate geologic unit. Modified from Michigan Department of Natural Resources.

1.2 Magnetic Terminology

To understand the research presented in this thesis, we define several magnetic terms. Curie Temperature (T_C) is a critical temperature at which thermal energy overcomes electronic exchange energy, resulting in randomization of electron spins (Moskowitz, 1991). T_C is related to mineral composition and therefore can be used in magnetic mineral identification. Coercivity relates to the ability of a magnetic material to resist changes in magnetization. A material with high coercivity that is difficult to re-magnetize is often expressed as 'hard' while a material with low coercivity that is easy to re-magnetize is often denoted as 'soft'. Coercivity is related to both magnetic mineral composition, as well as magnetic domain state.

A magnetic domain is defined by a uniform direction of magnetization that is influenced by the individual magnetic moments of atoms within the material. The domain state is affected by grain size. Superparamagnetic (SP) particles are uniformly magnetized, but are too small to support remanent (permanent) magnetization. Single domain (SD) particles are the smallest grain size that supports remanent magnetization, followed by pseudo-single domain (PSD), and finally the larger domain, multi-domain (MD) particles. In SP nanoparticles, thermal energy dominates, and they carry no remanence and therefore have no coercivity. SD grains are small enough that they are not capable of maintaining a domain wall, allowing these grains to be uniformly magnetized with high remanence and coercivity. MD grains are large enough that they can host a domain wall meaning that they are not uniformly magnetized. They have low remanence and coercivity and areas between domain walls are magnetically stable. PSD grains lack domain walls but have non-uniform magnetization, meaning they have characteristics similar to both SD and MD grains of high remanence but low coercivity (Moskowitz, 1991).

CHAPTER 2. BACKGROUND

2.1 General Overview of the Mid-Continent Rift and the Copper Harbor Conglomerate

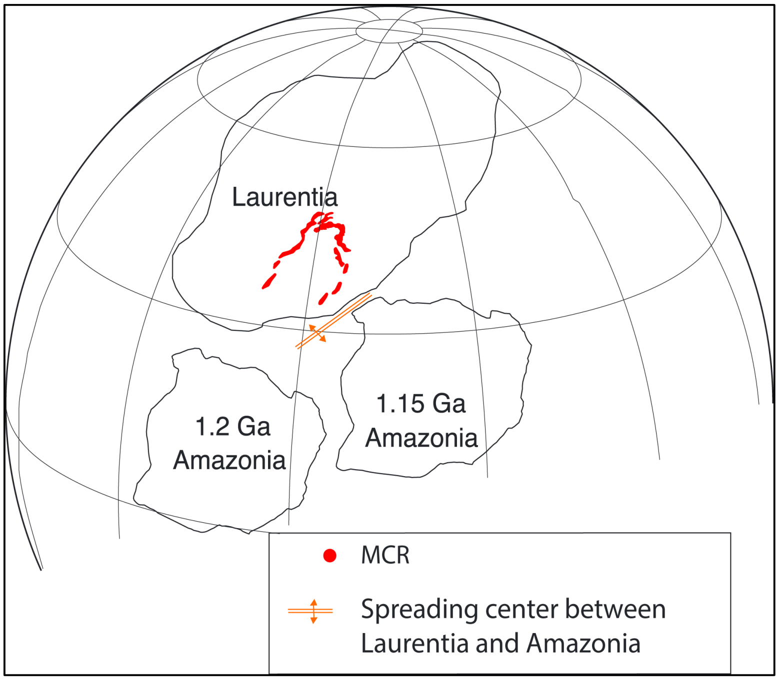

Figure 2: Separation of Amazonia from Laurentia

Depicts relationship between Amazonia and Laurentia, the spreading center between the two continents and the positioning of the MCR within the Laurentia Craton (~1.20-1.12 Ga). Modified from Stein et al. 2015.

During the Proterozoic, the continent Amazonia was separated from Laurentia by a strike-slip motion that began approximately 1.20 bya and lasted until 1.12 bya (Fig. 2; (Stein et al., 2014; Tohver et al., 2006). Seafloor spreading was established between the two continents as the shearing progressed, eventually separating them and ending the strain exerted on Laurentia. However, before the two cratons separated due to seafloor spreading, an internal rift developed within Laurentia (Stein et al., 2016). This relict feature is better known as the failed, Mid-Continent Rift (MCR) of modern day North America. The MCR feature is an approximately 3,000 km long, fault-bounded basin that extends from the Lake Superior region to the state of Kansas. The initial structure of the rift was dominated by faulting and subsidence related to extension. As the rift continued to develop, active rifting associated with a mantle plume contributed to the volcanic rocks that accompanied the MCR system (Fig. 3) (Stein et al., 2016). Sediments eventually infilled the basin primarily after the cessation of the extensional and volcanic interval of the MCR (Stein et al., 2016). The CHC sandstone of this study was part of the basin-margin alluvial fan system that deposited this sediment into the MCR basin approximately 1 bya. The CHC sandstone eventually fines into the lacustrine deposits of the Nonesuch Shale, which rests deeper into the MCR basin, which is identified as the Keweenawan Trough (Elmore, 1981).

2.2 General Background of the Copper Harbor Conglomerate Formation

The CHC rests upon the extinct MCR basin in the synclinal Keweenawan Trough of Lake Superior. This trough fully developed between 1.12-1.10 bya, following the cessation of rifting (Gordon and Hempton, 1986; Green, 1982). The base of the CHC overlies rocks associated with the Portage Lake Volcanics (PLV), which were active near the end of the extensional phase of the MCR and were the longest and most volumetrically significant volcanics related to the MCR (Ojakangas et al., 2001). The Lake Shore Trap (LST) volcanics followed the end of rift-related extension and interbed with the base of the CHC (Ojakangas et al., 2001). The LST represent the last volcanic activity associated with the failed MCR (Ojakangas et al., 2001).

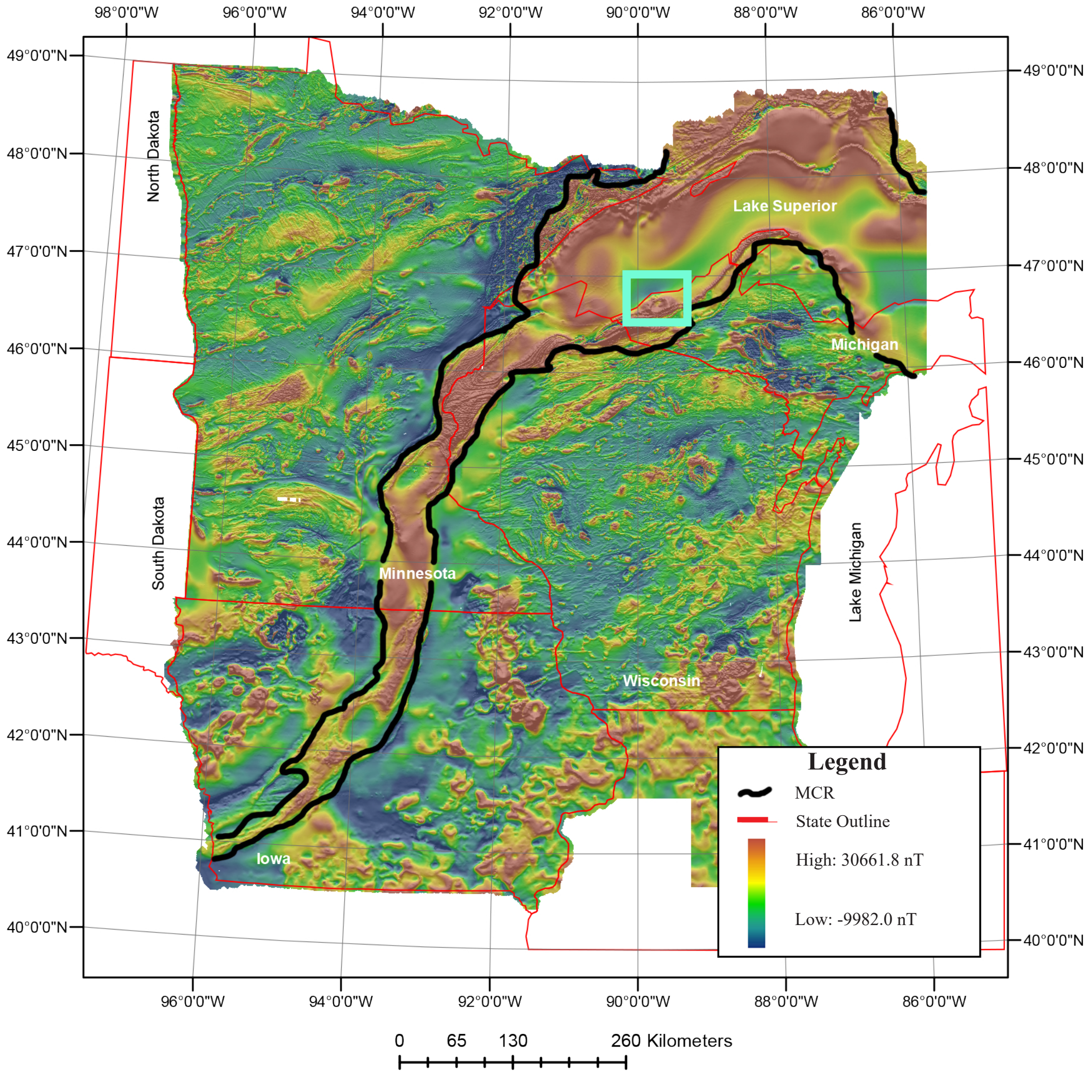

Figure 3: Aeromagnetic survey of the MCR

A gravity survey that demonstrates the extent of the MCR (outlined in black), the teal box designates the approximate location of the field study. Modified from United States Geological Survey from various sources.

The CHC is the lowest unit in the Oronto Group, a sedimentary unit generated by erosional deposits related to the Grenville orogeny and the formation of Rodinia (1.30-0.95 Ga) (Ojakangas et al., 2001; Stein et al., 2015). The sediments of the CHC originate primarily from the surrounding, predominantly volcanic rocks of the region (Elmore and van der Voo, 1982).

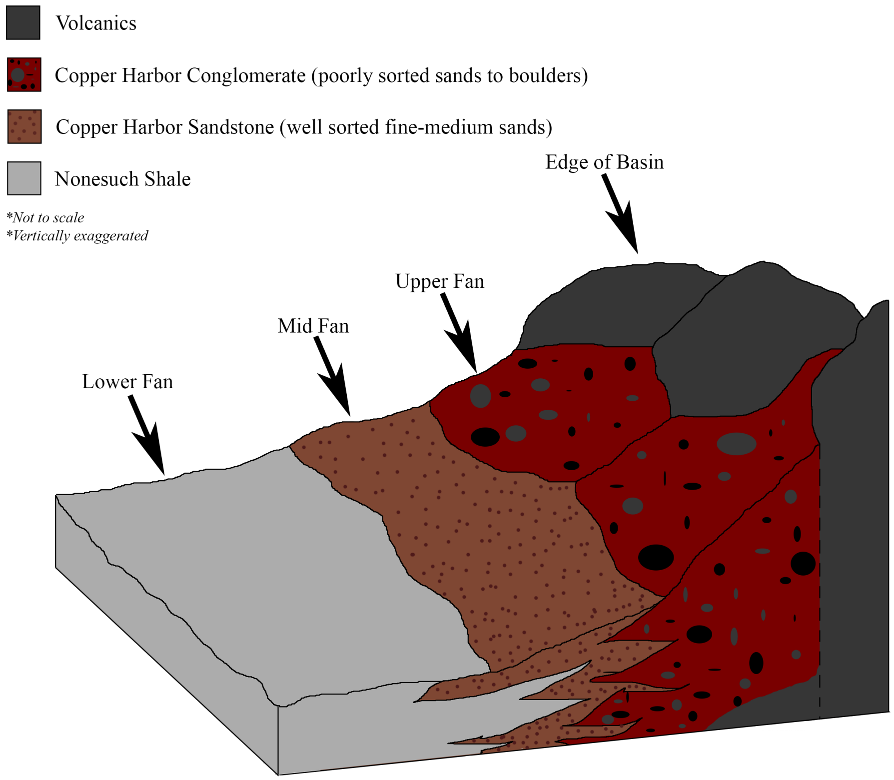

Figure 4: Depositional Setting within the Keweenawan Trough

Image depicts a typical depositional model for the transport and accumulation of sediments associated with basin fill of the MCR system.

The CHC sandstone facies is overlain by and interbedded with the lacustrine Nonesuch Shale, while the Freda Sandstone caps both units (Ojakangas et al., 2001). Figure 1 represents the juxtaposition of these units in the present geographic region of the field area for this study. It has been suggested that the transportation mechanism of CHC material was through alluvial and braided fan depositional systems that deposited debris in the rift basin during wet seasons (Fig. 4) (Wolff and Huber, 1973). Over the course of arid intervals, the dry sediment was interpreted to have been reworked by wind activity (Taylor and Middleton, 1990; Ojakangas et al., 2001). The CHC succession tends to fine upward and thicken basin-ward (Elmore, 1984). The base of the formation begins as a conglomerate with Keweenawan sourced volcanic clasts varying in size from sands to boulders (Ojakangas et al., 2001). Laterally, the conglomerate transitions to a red-brown, angular-sub-angular sandstone that alternates between medium- and fine-grained (Elmore, 1984; Bornhorst and Barron, 2013; Ojakangas et al., 2001).

2.3 Field Location Features and Descriptions

The conglomerate and sandstone of the CHC is exposed throughout the Keweenawan Peninsula and along the northern Michigan shoreline of Lake Superior (Elmore, 1984). Stratigraphic measurements discussed later in this study begin from the boat launch found on the shoreline of Lake Superior within the Union Bay campground. The general grain size identification of the outcrop exposure at Union Bay has been designated as well-sorted sandstones ranging from fine-to-medium grain-sizes that are angular to sub-angular (Wolff and Huber, 1973). Beginning from the boat launch location and moving up the section, stratigraphically, the first approximately 70 m are predominantly fine-grained, sublitharenite sandstones. This lower stratigraphic section, of fine-grained sandstones, primarily features dunes and cross-beds. It is important to note that fine-grained, cross-bedded sandstones featuring dunes are difficult to produce by unidirectional water flow (Moorhouse and White, 2016). Accretionary deposits such as bars, can produce cross-bed-like features, and fine sediment can produce cross-laminations due to ripple migration (Cheel, 2002). However, very fine sand cannot easily produce cross-bedding in dunes (Cheel, 2002), such as what we see at Union Bay. Throughout the entire outcrop exposure, there is a variety of depositional features including significant cross-stratification and trough-cross bedding associated with dunes, as well as parting lineation, climbing ripples, desiccation cracks, rip-up clasts, and ‘knobbly structures’. Taylor and Middleton (1990) referred to these knobbly structures as dewatering features but Noffke (2009) and Wilmeth et al. (2014) designated them to be microbial influenced sedimentary structures (MISS) that occurred on top of bedding planes. Around 70 m up-section, the grain size transitions to predominantly medium-grains with occasional coarse grain sandstone intervals. The grain size shift at approximately 70 m is also marked by thinner beds. Overall, the outcrops dip to the northeast (~21º) into and towards the central axis of the Keweenawan Trough which trends in a NE-SW direction through the middle of Lake Superior.

2.4 Magnetic Mineralogy and Paleomagnetic Overview of the Copper Harbor Conglomerate and The Local Volcanics

The CHC sediments primarily originated from erosion of the local volcanics, including the PLV, which were emplaced during and post extension of the MCR, and the LST volcanics, which occurred almost entirely during post extensional time (Ojakangas et al., 2001; Stein et al., 2015). To explain the magnetic mineralogy of the CHC, I therefore start with the volcanics from which the sediments were derived.

These regional volcanics have concentrations of magnetite and hematite, both of which carry magnetic remanence (Hnat et al., 2006; Kulakov et al., 2013). DuBois (1962) and Hnat et al. (2006) theorized that magnetite was a primary mineral of the PLV, and that hematite was a secondary mineral, formed via oxidation during cooling. This interpretation is supported by common directions for the magnetite (declination = 291.2°, inclination = 31.3°, α_{95} = 5.6º) and hematite (declination = 288.8º, inclination = 38.6º, α_{95} = 6.0º) magnetizations. This suggests that the magnetizations were acquired within a short time of cooling for both magnetic contributions

(Hnat et al., 2006). The LST also carries both soft (magnetite) and hard (likely hematite) components, with identical directions (declination = 277.8º, inclination = 41.0º, a_{95} = 2.3º) (Kulakov et al., 2013). Due to the directional similarities between the two components, it was inferred that the hematite formed via alteration of magnetite during the initial cooling of the LST (Kulakov et al., 2013).

Previous magnetic studies of the CHC found that the sandstone unit also has two magnetic remanence carriers: a low coercivity mineral inferred to be detrital magnetite that maintains a depositional remanence, and a high coercivity mineral interpreted to be mostly authigenic hematite that carries a secondary, post-depositional remanence (Elmore and van der Voo, 1982). There is a significantly larger fraction of hematite in the CHC relative to magnetite. Magnetite accounts for ~20-30% of the natural remanent magnetization (NRM), and its magnetization direction (declination = 294º, inclination = -7.6º) was isolated via the chemical demagnetization of the hematite component (declination = 286.5º, inclination = 0.0º) (Elmore and van der Voo, 1982). Inclination is correlated with bedding dip, suggesting that the magnetite remanence is depositional (Elmore and van der Voo, 1982). By contrast, the hematite inclination is not correlated with bedding dip, and the remanence direction of the hematite in the CHC is different from the magnetite direction and comparable with that of the overlying Freda Sandstone and Nonesuch Shale (Elmore and van der Voo, 1982). These observations support the interpretation that the hematite is indeed authigenic and therefore representative of a younger magnetic direction than that of magnetite (Elmore and van der Voo, 1982).

The exact nature and source of the hematite remanence is somewhat unclear, as previous studies found hematite present in multiple forms. The hematite present in the CHC at Union Bay is primarily found as ultrafine-pigmentary stain, martitized grains, or specularite oxide grains

(Elmore and van der Voo, 1982). The ultrafine-pigmentary hematite stain within the CHC either occurs as irregular clay coatings or uniform clay rims that exist between grain contacts (Elmore and van der Voo, 1982). The uniform clay coatings would have developed prior to deposition, the clay platelets found in these uniform rims was likely a product from the weathering and dehydration of iron-bearing silicates (Elmore and van der Voo, 1982). Meanwhile the irregular clay coatings that present as a box-work texture are inferred to have formed in place, post-depositionally, within the interstitial spaces between grains (Elmore and van der Voo, 1982). The ultrafine-pigmentary hematite of the clay rims, whether pre- or post-deposition, was inferred to be mostly superparamagnetic (SP) in size and should not be able to carry a magnetic remanence. However, a wide range of blocking temperatures was observed in samples from the CHC, which indicates that fine-grained hematite likely carries a significant amount of the magnetic remanence (Elmore and van der Voo, 1982). The wide range of blocking temperatures is likely attributed to variable magnetic grain sizes. Hematite of possible authigenic or detrital origin exists within the CHC either as post-depositional martite grains or pre-depositional martite found in volcanic fragments (Elmore and van der Voo, 1982). Martite is a pseudo-morph of magnetite that maintains the habit of magnetite, despite altering into hematite, and some of the CHC martite grains maintain relict magnetite (Elmore and van der Voo, 1982; Vincenz, 1968). Martite found in local volcanics from which the CHC was sourced support its presence within the CHC as detrital. However, Elmore and van der Voo (1982) suggest that at least some of the martite transformed post-depositionally. Although the ~1μm specularite oxide grains may be depositional, Elmore and van der Voo (1982) similarly suggested that these are authigenic and therefore carry a secondary remanence.

Because our study is not concerned with remanence, we shift our focus to what contributes to magnetic susceptibility. Susceptibility measures the total response to an induced magnetic field, and reflects all magnetic minerals. Magnetic susceptibility is typically influenced by mineralogy, grain size, or concentration. Elmore and van der Voo (1982) observed detrital magnetite, martite, and specularite as well as authigenic pigmentary hematite clay rims and coarse hematite crystal grains. Whether the hematite is authigenic or detrital, fine or coarse grained, due to its significant abundance in the CHC it is likely that its presence will be a dominant factor for susceptibility measurements. Therefore, one of our primary goals is to determine if susceptibility measurements are representative of a depositional signal for this unit.

CHAPTER 3. METHODS

3.1 Block Sampling

Three field excursions were conducted, the first in August of 2016, the second in May of 2017, and the third in August of 2017. During the first field season (August 2016), fifteen pilot samples were acquired with a rock hammer and chisel from field Locality 1 and 2 (Fig. 1). The second field season (May and August 2017), twenty-nine additional samples were acquired only from field Locality 1. The samples for both field seasons were all hand size, orientated block samples, weighing approximately 1-3 lbs individually, and not exceeding 30 x 20 cm. Samples were oriented with a Brunton magnetic compass, and strike and dip were marked on the sample. In accordance with our permit granted by the Michigan Department of Natural Resources for use of State Land, samples were collected along the shoreline outcrops of the CHC next to Union Bay Campground, within The Porcupine Wilderness State Park, Michigan. The pilot samples of the first field season were selected from two different Localities. Locality 1 (Fig. 1) samples were selected based upon unique bedding features that included depositional varieties of fine laminations, presence of MISS, ripples, rip-up clasts, mud cracks, trough cross-bedding, and proximity to conglomerate beds or parting lineation bedforms. Locality 2 was ~21 km west of the campground, and was selected due to the relatively larger grain size and the amount of heavy physical weathering that had occurred at the location. Following initial testing of the fifteen pilot samples, Locality 2 was not resampled during the subsequent season. The second field season focused sampling at Locality 1 to within the first 60 stratigraphic meters from the boat launch. We obtained supplementary, oriented block samples that were sparsely spaced throughout the section. These block samples were taken on average every 2.67 stratigraphic meters, at minimum intervals of 0.09 m and maximum intervals of 26.8 m.

3.2 Naming Convention

To interpret the legends and plots described in this thesis, please reference our naming convention. Locations are defined by CH16 and CH17, CH stands for Copper Harbor while 16 and 17 stand for 2016 and 2017 field seasons, respectively. The sampling locality is denoted as either 01 or 02 directly following the location sequence. Each block sample taken has a unique sample number, denoted by the last two numbers in the sequence, ranging from 01 – 29. Each sample was subdivided into specimens, indicated by a letter at the very end of the numbered sequence. For example, CH160103a represents specimen ‘a’ taken from sample 3, collected from Locality 1 during the 2016 field season. The only exceptions to this naming convention are CH160102b and CH170110s. These are secondary samples taken at the same time as Sample 2 during the 2016 season and Sample 10 during the 2017 season, respectively.

3.3 Outcrop Susceptibility Measurements

To conduct outcrop susceptibility measurements, the KT-10 v2 S/C Magnetic Susceptibility Meter was used. The meter has an operating frequency of 10kHz, a susceptibility sensitivity of 1×10^{-6} SI units, and a susceptibility range of 0.001×10^{-3} to 1999.99×10^{-3} SI units. Magnetic susceptibility (χ) is a physical property that conveys the extent to which a material becomes magnetized in the presence of a field. $\chi = M/H$, M=intensity of magnetization and H=magnetic field. The KT-10 meter applies an alternating field and derives susceptibility from the response frequency difference between the outcrop and the free-air. The susceptibility meter averages over a distance of 65 mm which is the diameter of the meter's coil.

3.3.1 Stratigraphic Susceptibility Measurement Collection

Along the Lake Superior shoreline in Union Bay State Park of the Porcupine Wilderness, Michigan, stratigraphic susceptibility measurements were collected. These measurements were obtained to achieve high-resolution information due to the necessarily sparse physical sample collection permitted at this outcrop location. Accurate spectral analysis of the stratigraphic variations in susceptibility requires frequent measurements that are evenly spaced and accurately located. Our measurement strategy was to sample approximately every 0.5 m. However, because outcrop along the lake was not continuous and dipped into the lake, there were both occasional gaps in the sampling and likely some error in measuring the section. Measurements were made by pressing the susceptibility meter flush against the outcrop to measure the magnetic susceptibility at each location. Stratigraphic measurements were taken a minimum of every 0.01 m and a maximum distance of 1.5 m apart in stratigraphic height, with an average spaced interval of 0.47 m. These susceptibility readings were taken up-section, stratigraphically, over a total of 56.4 m. A minimum of three measurements were taken at each measurement location to estimate uncertainty. Good contact between the susceptibility-meter and outcrop is required for accurate readings, and clear outlier measurements were discarded.

3.3.2 Stratigraphic Susceptibility Data Analysis

A spectral analysis of the susceptibility data series was conducted following the protocol outlined by Kodama and Hinnov (2015). First, the data series was resampled at the average sampling rate of 0.47 m using a simple linear interpolation (Kodama et al., 2010). A linear trend was removed from the data series using Matlab^{TM} polynomial curve fitting and evaluation. The multitaper spectral analysis of the data utilized a set of 5, 3π Slepian tapers following Matlab function *pmtm.* Tapers are regulated by mathematical functions that define the shape of a data window (Kodama and Hinnov, 2015). Data windows are used to isolate time series data by dropping all values outside of the defined window to zero and the smoothness or sharpness of the window edge is defined by the taper function used (Kodama and Hinnov, 2015). Multiple Slepian tapers were used, each taper functions independently of the others, but when all tapers are summed together they approximate the simplest data window, the Dirichlet window (Kodama and Hinnov, 2015). Due to the greater uncertainty in the positioning of our data, we used the 3π Slepian taper rather than the 2π Slepian taper that was recommended by Kodama et al. (2010) to assist with greater smoothing of our data. The greater smoothing diminishes the spectral resolution but increases confidence in the spectral peaks. Significance of the spectral peaks was estimated by performing a Monte Carlo simulation (N=1000) of a red noise spectrum, using Matlab code developed by D. Husson (available from https://www.mathworks.com/matlabcentral/fileexchange/45539-rednoise-confidencelevels) and resulted in 80%, 85%, 90%, and 99% confidence limits. Elevation of data spectral peaks above the red noise background level suggests these frequency peaks are not noise. The red noise spectrum is thought to best represent climate and geological time series (Kodama and Hinnov, 2015). Red noise gives greater power to lower frequency rather than high frequency noise, and unlike white noise spectrums that are completely independent of frequency behavior, red noise retains a “memory” (Kodama and Hinnov, 2015). This memory means that prior behavior influences future behavior (Kodama and Hinnov, 2015).

3.3.3 Small Scale Outcrop Susceptibility Measurement Collection

To examine variability at length scales < 0.5 m, two separate grid sections were established to measure susceptibility variations within bed-forms. Grid 1 (46º49’22.45” N, 89º38’19.12” W) was mapped out on a flat outcrop surface with a grid system measuring 90 x 40 cm. The grid was sectioned off into 5 x 5 cm squares, which created eight columns vertically down the grid labeled A-H, and eighteen rows horizontally across the grid labeled 1-18. Susceptibility was measured within each 5 x 5 cm square. Grid 2 (46º49’22.45” N, 89º38’19.12” W) was also mapped adjacent to Grid 1 on the same outcrop. This grid was mapped out in an irregular rectangular shape to avoid rough sections of the outcrop that would not permit for direct contact between the rock and the susceptibility-meter. The horizontal length of the grid was 310 cm, and the vertical extent varied from 170 cm on the left to 230 cm on the right. Vertically from top-to-bottom, susceptibility measurements were taken every 5 cm. Horizontally from left-to-right, susceptibility measurements were taken every 10 cm. In accordance with earlier susceptibility recordings, a minimum of three measurements were taken at each point within both grids to establish an average reading of susceptibility.

3.4 Hand Sample Laboratory Methods

3.4.1 Sample Preparation

From the pilot samples obtained during the initial field season, four individually oriented ~1x1x1 inch cube specimens were cut from all samples using a table saw with a 6” blade. Four specimens were cut from each sample block, resulting in 60 total specimens. Prior to cutting, the strike and dip of the block sample was transferred across the rock surface so that outcrop position could be maintained during laboratory analysis. NRM, room-temperature bulk susceptibility (χ_B), and anisotropy of magnetic susceptibility (AMS) were measured on all four specimens from each sample. One specimen set was subjected to detailed isothermal remanent magnetization (IRM) step-acquisition up to 1 T, followed by a single back-field IRM at 0.3 T. Curie temperatures (T_C) were measured on additional crushed material from the pilot samples. The coarsely crushed specimen splits were placed into a quartz tube when measured by the CS4 furnace attachment of the MFK1 Kappabridge.

The 29 samples obtained during the second field season were prepared in the same fashion as those from the initial field season. However rather than creating four sets of specimens, only one set was required for laboratory measurements. The excess from the cut samples was retained for alternate or future sample testing. The same tests were also performed, except for the detailed IRM acquisition and T_C measurements.

3.4.2 Laboratory Instrumentation

All remanence measurements for both the pilot and subsequent specimens were conducted on a 2G Enterprises 755SRMS Superconducting Rock Magnetometer housed inside the shielded room at the University of Wisconsin-Milwaukee Paleomagnetic Laboratory. χ_B and AMS were measured on an Agico MFK1 Kappabridge susceptibility bridge. Susceptibility was measured as a function of temperature, $\chi(T)$, on coarsely crushed splits from each pilot sample. This was carried out using the CS4 furnace attachment for the MFK1 Kappabridge under air atmosphere. Curie temperatures were estimated by taking the peak in the first derivative of the $\chi(T)$ data after applying a furnace correction and smoothing the data with a running-mean filter.

3.4.3 Chemical Demagnetization

Pilot specimen sets 3 and 4 were retained for additional resources or future testing not included in this research. Pilot specimen set 1 was subjected to chemical demagnetization with the intention of isolating detrital magnetite. This process involved the submersion of each specimen into 3N HCl solution, with the purpose of preferentially dissolving the fine-grained pigmentary hematite. The leaching process was monitored by measuring magnetization at 3-day intervals for a total of 480 hours. The leaching process was abandoned after 480 hours due to the small amount of remanence that was removed during the process.

3.4.4 Isothermal Remanent Magnetization (IRM) Acquisition

Pilot specimen set 2 was alternating field (AF) demagnetized using an ASC D-2000 Alternating Field Demagnetizer up to peak fields of 200 mT. However, the high-coercivity hematite proved resistant to demagnetization. Samples from Locality 1 lost 26.12% ± 8.19% NRM on average, and Locality 2 lost 59.43% ± 1.23% NRM on average. Next, the specimens acquired a 20-step isothermal remanent magnetization (IRM) up to a 1 T field using an ASC Model IM10-30 impulse magnetizer (IRM steps were applied at 5, 10, 15, 20, 25, 30, 40, 50, 60, 80, 100, 125, 150, 200, 250, 300, 400, 600, 800, and 1000 mT). Following the final step at a 1T field, a backfield 300 mT IRM was acquired to enable calculation of the S-ratio and Hard-IRM. Samples from the second field season were only given the 1T forward IRM and the 300 mT backfield IRM. We use the S-ratio definition of $-\text{IRM}_{-300\text{mT}}/\text{IRM}_{1\text{T}}$ where $\text{IRM}_{-300\text{mT}}$ is the backfield 300 mT IRM following application of the forward 1 T field (Liu et al., 2012). When an S-ratio is near 1 the data would be representative of a greater proportion of soft minerals within the sample, such as magnetite, while a value near -1 would be indicative of harder minerals such as hematite. We calculate the $\text{Hard-IRM} = 0.5 \text{ x } (\text{IRM}_{1\text{T}} + \text{IRM}_{-300\text{mT}})$ and the $\text{Soft-IRM} = \text{IRM}_{1\text{T}} - \text{Hard-IRM}$. Respectively, these represent the portion of the IRM carried by high-coercivity and low-coercivity magnetic minerals.

IRM acquisition data from the pilot specimens was decomposed in terms of their coercivity spectra to tease out variations in different populations of magnetic grains. We apply this technique to the first derivative of the IRM vs. applied field data, following methodology developed by Robertson and France (1994), Stockhausen (1998), Kruiver et al. (2001), Heslop et al. (2002), Egli (2003), Heslop and Dillion (2007), and Heslop (2015), modified by Maxbauer et al. (2016). The MAX UnMix web application fits a set of skew-normal functions to the observed coercivity distribution as determined by the first derivative of the log data curves (Maxbauer et al., 2016). The program requires a bit of subjectivity as the user determines the number of components and identifies the preliminary characteristics of the distributions (Maxbauer et al., 2016). After the user completes the initial fit for the data, the program will refine the model to minimize any misfit to the data (Maxbauer et al., 2016). A complete explanation of this program is found at http://www.irm.umn.edu/maxunmix or in Maxbauer et al. (2016).

Each of the pilot specimen's IRM data sets was imported into the MAX UnMix website program. The data were then smoothed with a smoothing spline that assists with curve fitting at ranges between 0 (no smoothing), to 1 (maximum smoothing) (Maxbauer et al., 2016). The smoothing factor that was applied to the IRM acquisition curves of the pilot samples was 0.3 and was utilized to remove excessive noise from the set which becomes amplified from taking the first derivative.

3.4.5 Anisotropy of Magnetic Susceptibility (AMS)

AMS is determined by the directional relationship between a magnetic field and induced magnetization. AMS is frequently used to estimate the alignment of magnetic minerals within a specimen or site by measuring how the magnitude of susceptibility changes with orientation to an applied field. This characteristic is made possible by minerals that have a shape anisotropy which affects the easy axis of magnetization.

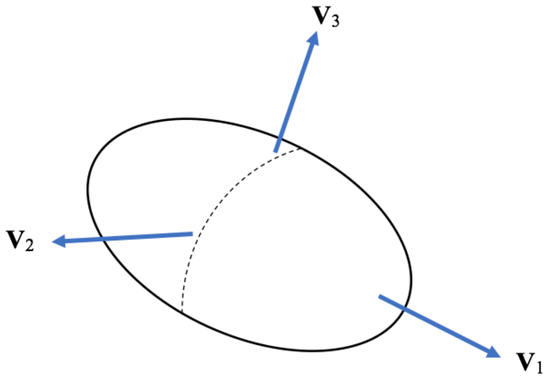

Figure 5: Orientation of eigenvectors
Modified from Tauxe, 2016.

Anisotropy is described by a second rank tensor. The eigenvalues and eigenvectors of this tensor can be represented by an ellipsoid with three principal axes that correspond to the maximum (easy), intermediate, and minimum (hard) directions of magnetization. The lengths of the axes are determined by eigenvalues, τ_1 (maximum), τ_2 (intermediate), and τ_3 (minimum). The directions of the principal axes are given by the eigenvectors $\mathbf{V}_1$ (maximum), $\mathbf{V}_2$ (intermediate), and $\mathbf{V}_3$ (minimum) (Figure 5). The shape of an ellipsoid can be characterized as spherical (isotropic, $\tau_1=\tau_2=\tau_3$), oblate ($\tau_1=\tau_2>\tau_3$), prolate ($\tau_1>\tau_2=\tau_3$), or triaxial ($\tau_1>\tau_2>\tau_3$) (Tauxe, 2016; Fig. 6).

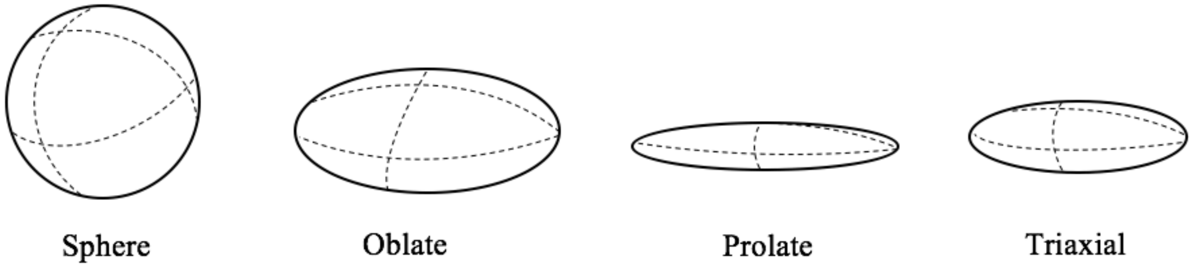

Figure 6: Magnetic shapes as determined by their eigenvalues
Modified from Tauxe, 2016.

A typical sedimentary fabric for sediments deposited in quiet, standing water is an oblate shape with the $\mathbf{V}_3$ oriented perpendicular to the bedding (Tauxe, 2016). When slow-moving currents are responsible for deposition, once again the AMS shape will be oblate, but the grains will be slightly imbricated with $\mathbf{V}_3$ shifted slightly away from a vertical orientation (Tauxe, 2016). Typically, very fast moving or turbulent flow will create a prolate or triaxial AMS fabric (Tauxe, 2016). High energy deposition may result in grains rolling with their long axes perpendicular to flow direction. In this case, $\mathbf{V}_3$ axes will appear smeared across a stereonet plot and the orientation of $\mathbf{V}_1$ will be perpendicular to the direction of paleo-flow (Tauxe, 2016). However, in the case of less turbulent, more moderate water flow, magnetic grains will orient with their long axes parallel to flow direction (Tauxe, 2016). Both sets of specimens from the pilot sampling and secondary field season were subjected to measurement of AMS.

CHAPTER 4. RESULTS

4.1 Overview of Laboratory Magnetic Measurements

All measured samples from both field seasons had two magnetic components, one high and one low coercivity. Both NRM and χ_B were relatively constant; the mean NRM was $1.35 \pm 0.58 \times 10^{-2}$ Am^2/kg and the mean χ_B was $1.21 \pm 0.21 \times 10^{-7}$ m^3/kg. Heating curve Curie temperatures (T_C) ranged from 550-572ºC, suggestive of low-Ti titanomagnetite, while approximately half had an additional T_C in the range of 600-680ºC, suggestive of titanohematite. Refer to Table 1 for a complete compilation of characteristics pertaining to T_C, NRM, χ_B, and IRM un-mixing of the pilot samples from the initial field season (2016). Refer to Table 2 for a compilation of characteristics pertaining to NRM, χ_B, IRM un-mixing, and relative stratigraphic height of the subsequent samples from the second field season (2017). Raw IRM, $\chi(T)$, and AMS data have been archived in the Magnetics Information Consortium (MagIC) database (earthref.org/MagIC).

Table 1: CH16 bulk-magnetic properties

Specimen ID	S-ratio	IRM_{1T} (Am^2/kg)	Hard IRM (Am^2/kg)	Soft IRM (Am^2/kg)	NRM (Am^2/kg)	χ_B (m^3/kg)	T_C (°C) Heating	T_C (°C) Cooling	Color Change $\chi(T)$	Irreversible $\chi(T)$
CH160101A	-3.74×10^{-1}	9.91×10^{-3}	6.81×10^{-3}	3.10×10^{-3}	1.89×10^{-2}	1.49×10^{-7}	569	558	Black	Y
CH160102A	-3.48×10^{-1}	7.46×10^{-3}	5.03×10^{-3}	2.43×10^{-3}	1.36×10^{-2}	1.20×10^{-7}	572	561	Black	Y
CH160102BA	-3.23×10^{-1}	7.33×10^{-3}	4.84×10^{-3}	2.48×10^{-3}	3.84×10^{-2}	1.15×10^{-7}	569 & 680	575	Tan	Y
CH160103A	-1.79×10^{-1}	7.62×10^{-3}	4.49×10^{-3}	3.13×10^{-3}	9.63×10^{-3}	1.10×10^{-7}	395, 550-590, & 650	573 & 660	Red	N
CH160104A	-2.48×10^{-1}	5.84×10^{-3}	3.64×10^{-3}	2.19×10^{-3}	1.27×10^{-2}	8.98×10^{-8}	495, 565, & 650	478 & 550	Red	N
CH160105A	-3.09×10^{-1}	4.78×10^{-3}	3.13×10^{-3}	1.65×10^{-3}	9.02×10^{-3}	9.36×10^{-8}	565	578	Tan	Y
CH160106A	3.30×10^{-1}	6.40×10^{-3}	4.26×10^{-3}	2.15×10^{-3}	1.25×10^{-2}	1.09×10^{-7}	575	556	Black	Y
CH160107A	-3.29×10^{-1}	3.91×10^{-3}	2.60×10^{-3}	1.31×10^{-3}	2.30×10^{-2}	9.78×10^{-8}	560 & 650	561	Red	N
CH160108A	-2.71×10^{-1}	3.56×10^{-3}	2.26×10^{-3}	1.30×10^{-3}	7.34×10^{-3}	9.46×10^{-8}	550 & 680	582	Red	Y
CH160109A	-1.82×10^{-1}	3.83×10^{-3}	2.26×10^{-3}	1.56×10^{-3}	1.28×10^{-2}	9.50×10^{-8}	550 & 637	550 & 647	Red	N
CH160110A	-3.58×10^{-1}	9.12×10^{-3}	6.19×10^{-3}	2.93×10^{-3}	1.08×10^{-2}	1.46×10^{-7}	561 & 600	568	Red	N
CH160111A	-2.61×10^{-1}	5.65×10^{-3}	3.56×10^{-3}	2.09×10^{-3}	2.14×10^{-2}	1.12×10^{-7}	560	569 & 650	Red	N
CH160112A	-3.48×10^{-1}	9.34×10^{-3}	6.30×10^{-3}	3.04×10^{-3}	1.29×10^{-2}	1.43×10^{-7}	550 & 632	400, 575, & 629	Red	N
CH160201A	-2.27×10^{-1}	8.27×10^{-3}	5.07×10^{-3}	3.20×10^{-3}	8.26×10^{-3}	1.84×10^{-7}	563	571	Dark Red	Y
CH160202A	-2.29×10^{-1}	6.90×10^{-3}	4.24×10^{-3}	2.66×10^{-3}	2.83×10^{-2}	1.63×10^{-7}	565	570	Dark Red	Y

Table 1: The S-ratio, SIRM, Hard-IRM, and Soft-IRM concluded that high coercivity, hard minerals such as hematite dominated the magnetic remanence of the CHC. This table represents the magnetic characteristics of the CHC including: the natural remanent magnetization prior to any testing (NRM), the Curie temperatures identified on heating and cooling (T_C), the bulk susceptibility (χ_B), if a color change occurred during the high temperature susceptibility procedure ($\chi(T)$), and whether the $\chi(T)$ curves were strongly irreversible

Table 2: CH17 bulk magnetic properties

Specimen ID	S-ratio	IRM$_{1T}$ (Am^2/kg)	Hard IRM (Am^2/kg)	Soft IRM (Am^2/kg)	NRM (Am2/kg)	χ_B (m^3/kg)	Stratigraphic Height (m)
CH170101A	-3.50 x 10^{-1}	6.30 x 10^{-3}	4.25 x 10^{-3}	2.05 x 10^{-3}	8.80 x 10^{-3}	1.13 x 10^{-7}	14.4
CH170102A	-3.51 x 10^{-1}	6.51 x 10^{-3}	4.40 x 10^{-3}	2.11 x 10^{-3}	9.08 x 10^{-3}	1.12 x 10^{-7}	16.0
CH170103A	-2.41 x 10^{-1}	5.48 x 10^{-3}	3.40 x 10^{-3}	2.08 x 10^{-3}	1.01 x 10^{-2}	1.11 x 10^{-7}	16.0
CH170104A	-2.45 x 10^{-1}	4.85 x 10^{-3}	3.02 x 10^{-3}	1.83 x 10^{-3}	8.66 x 10^{-3}	9.45 x 10^{-8}	19.0
CH170105A	-3.24 x 10^{-1}	6.62 x 10^{-3}	4.38 x 10^{-3}	2.24 x 10^{-3}	9.97 x 10^{-3}	1.22 x 10^{-7}	21.6
CH170106A	-3.87 x 10^{-1}	4.90 x 10^{-3}	3.40 x 10^{-3}	1.50 x 10^{-3}	9.91 x 10^{-3}	1.14 x 10^{-7}	26.0
CH170107A	-4.95 x 10^{-1}	6.67 x 10^{-3}	4.99 x 10^{-3}	1.68 x 10^{-3}	1.63 x 10^{-2}	1.39 x 10^{-7}	26.1
CH170108A	-6.09 x 10^{-1}	4.75 x 10^{-3}	3.83 x 10^{-3}	9.29 x 10^{-4}	1.43 x 10^{-2}	1.29 x 10^{-7}	26.7
CH170109A	-4.12 x 10^{-1}	6.71 x 10^{-3}	4.74 x 10^{-3}	1.97 x 10^{-3}	1.44 x 10^{-2}	1.37 x 10^{-7}	26.8
CH170110A	-3.97 x 10^{-1}	4.86 x 10^{-3}	3.39 x 10^{-3}	1.47 x 10^{-3}	9.92 x 10^{-3}	1.18 x 10^{-7}	29.1
CH170110SA	-4.04 x 10^{-1}	5.06 x 10^{-3}	3.55 x 10^{-3}	1.51 x 10^{-3}	7.84 x 10^{-3}	1.23 x 10^{-7}	29.1
CH170111A	-3.53 x 10^{-1}	8.04 x 10^{-3}	5.44 x 10^{-3}	2.60 x 10^{-3}	1.35 x 10^{-2}	1.37 x 10^{-7}	30.2
CH170112A	-5.42 x 10^{-1}	5.40 x 10^{-3}	4.16 x 10^{-3}	1.24 x 10^{-3}	1.30 x 10^{-2}	1.41 x 10^{-7}	30.7
CH170113A	-3.92 x 10^{-1}	4.74 x 10^{-3}	3.30 x 10^{-3}	1.44 x 10^{-3}	1.08 x 10^{-2}	1.16 x 10^{-7}	34.7
CH170114A	-2.43 x 10^{-1}	5.32 x 10^{-3}	3.31 x 10^{-3}	2.01 x 10^{-3}	9.26 x 10^{-3}	1.09 x 10^{-7}	35.5
CH170115A	-2.51 x 10^{-1}	6.56 x 10^{-3}	4.10 x 10^{-3}	2.46 x 10^{-3}	1.06 x 10^{-2}	1.06 x 10^{-7}	37.0
CH170116A	-1.50 x 10^{-1}	6.12 x 10^{-3}	3.52 x 10^{-3}	2.60 x 10^{-3}	1.15 x 10^{-2}	1.14 x 10^{-7}	39.0
CH170117A	-3.70 x 10^{-1}	6.03 x 10^{-3}	4.13 x 10^{-3}	1.90 x 10^{-3}	1.65 x 10^{-2}	1.27 x 10^{-7}	40.6
CH170118A	-2.68 x 10^{-1}	5.59 x 10^{-3}	3.55 x 10^{-3}	2.05 x 10^{-3}	7.49 x 10^{-3}	9.71 x 10^{-8}	43.3
CH170119A	-2.69 x 10^{-1}	5.01 x 10^{-3}	3.18 x 10^{-3}	1.83 x 10^{-3}	6.98 x 10^{-3}	1.03 x 10^{-7}	45.2
CH170120A	-4.39 x 10^{-1}	6.27 x 10^{-3}	4.51 x 10^{-3}	1.76 x 10^{-3}	1.44 x 10^{-2}	1.52 x 10^{-7}	47.5
CH170121A	-3.33 x 10^{-1}	6.29 x 10^{-3}	4.19 x 10^{-3}	2.10 x 10^{-3}	7.34 x 10^{-3}	1.20 x 10^{-7}	48.9
CH170123A	-4.56 x 10^{-1}	4.52 x 10^{-3}	3.29 x 10^{-3}	1.23 x 10^{-3}	1.05 x 10^{-2}	1.18 x 10^{-7}	50.7
CH170124A	-4.15 x 10^{-1}	5.27 x 10^{-3}	3.73 x 10^{-3}	1.54 x 10^{-3}	1.32 x 10^{-2}	1.21 x 10^{-7}	52.7
CH170125A	-3.28 x 10^{-1}	6.26 x 10^{-3}	4.15 x 10^{-3}	2.10 x 10^{-3}	8.50 x 10^{-3}	1.16 x 10^{-7}	53.7
CH170126A	-3.09 x 10^{-1}	5.51 x 10^{-3}	3.61 x 10^{-3}	1.90 x 10^{-3}	6.15 x 10^{-3}	1.14 x 10^{-7}	54.2
CH170127A	-4.82 x 10^{-1}	5.59 x 10^{-3}	4.14 x 10^{-3}	1.45 x 10^{-3}	1.30 x 10^{-2}	1.30 x 10^{-7}	55.4
CH170128A	-3.09 x 10^{-1}	8.12 x 10^{-3}	5.31 x 10^{-3}	2.81 x 10^{-3}	1.65 x 10^{-2}	1.20 x 10^{-7}	55.9

Table 2: The S-ratio, SIRM, Hard-IRM, and Soft-IRM concluded that high coercivity, hard minerals such as hematite dominated the magnetic remanence of the CHC. Magnetic characteristics of the CHC are listed as well including the natural remanent magnetization prior to any testing (NRM), the bulk susceptibility (χ_B), and their stratigraphic height relative to the boat launch at Union Bay Campground.

4.2 Chemical Demagnetization

Overall very little remanence was lost through the chemical demagnetization process. On average, a total of 1.70% ± 2.76% of the NRM was removed after the full 480 hours. A range of 5.75% of original NRM was removed and 4.41% remanence was gained during the leaching process. Ultimately, chemical demagnetization had very little effect on remanence. Elmore and van der Voo (1982) successfully removed 50-80% of the total NRM through chemical demagnetization. They saw the greatest reduction in magnetization within the first 400 hours (Elmore and van der Voo, 1982). Despite Elmore and van der Voo's (1982) success, our chemical demagnetization process was determined to not be a practical method to isolate the NRM associated with the magnetite component. We speculate that Elmore and van der Voo (1982) saw a more favorable outcome for the removal of the NRM due to their higher strength solution (10N HCl) and due to their specimen preparation (2.2 cm height cores with additional slots cut into the specimens). The slots cut into their specimens provided greater direct surface area to be in contact with the HCl solution, this may have been easier for the acid to permeate, resulting in a greater amount of dissolved hematite. Since the NRM is not the focus of our study, this line of inquiry was dropped.

4.3 Susceptibility as a Function of Temperature, $\chi(T)$

The T_C identified on heating varied widely between 395 to 637 ºC. However, as noted above (Table 1), all samples had a T_C on heating in the range near pure magnetite (580°C). Approximately half of the data displayed $\chi(T)$ with strong irreversibility, reflected in a large increase in susceptibility on cooling, a strong magnetite peak on cooling, and a color change from the original purple-red of the sample to black. These qualities suggest that the hematite thermo-chemically altered to magnetite during measurement. Such a transformation requires a reducing atmosphere, and although measurements were not made under flowing inert gas, they also were not made under flowing air. This suggests that any oxygen in the sample chamber at the beginning of the experiment was consumed during the experiment. Hopkinson peaks associated with magnetite were frequently observed on cooling curves but not on warming curves, primarily on samples that demonstrated significant irreversibility for $\chi(T)$. A Hopkinson peak is marked by a sharp, steep increase in susceptibility just below the Curie temperature. The Hopkinson peak marks a sudden increase in susceptibility between the blocking temperature (T_B) and T_C that is often associated with finer magnetic grain sizes (Tauxe, 2016). This characteristic suggests that the newly-formed magnetite is of SD grain sizes.

The temperature dependent susceptibility measured from the coarsely crushed specimen splits is relatively low, contributing to uncertainty and noise in the analysis. For comparison, data measured with no specimen loaded (empty furnace and sample tube) is shown in Appendix 1. The quartz sample, ceramic furnace assembly, and plastic cooling water jacket are all made of diamagnetic materials that have no magnetic remanence. However, when exposed to a magnetic field diamagnetic materials have a small induced magnetization opposite to the applied field regardless of temperature (Butler, 2004). Although the diamagnetic signal should be invariant with temperature, some component of the furnace assembly clearly has a temperature-dependent signal between ~500-700 °C (Appendix 1). This signal is subtracted from the measured specimen data, but in some cases the specimen signal is barely above the background, resulting in some uncertainty in interpretation.

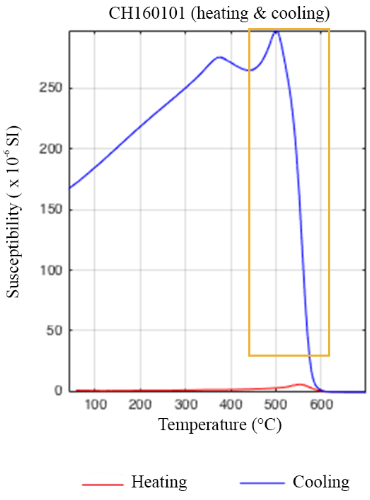
CH160101 (heating & cooling)
Susceptibility (x 10⁻⁶ SI)
250
200
150
100
50
0
100
200
300
400
500
600
Temperature (°C)
Heating
Cooling

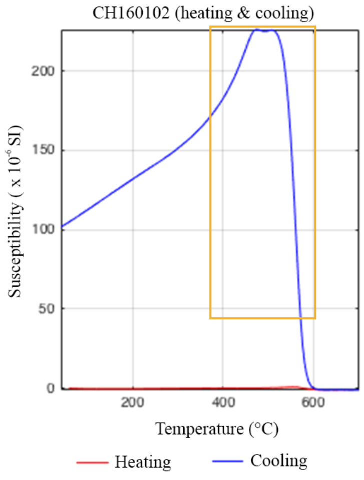
CH160102 (heating & cooling)
Susceptibility (x 10⁻⁶ SI)
200
150
100
50
0
200
400
600
Temperature (°C)
Heating
Cooling

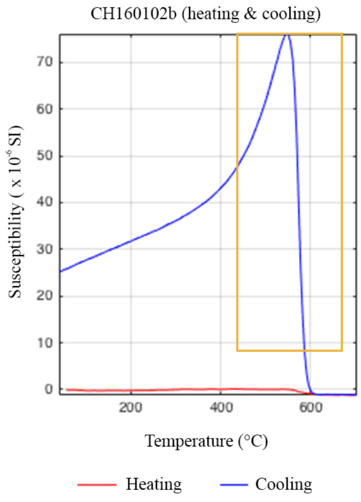
CH160102b (heating & cooling)
Susceptibility (x 10⁻⁶ SI)
70
60
50
40
30
20
10
0
200
400
600
Temperature (°C)
Heating
Cooling

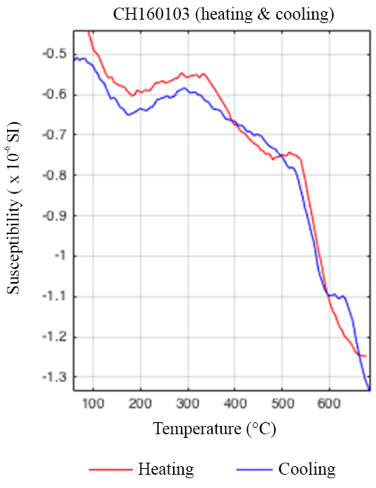
CH160103 (heating & cooling)
Susceptibility (x 10⁻⁶ SI)
-0.5
-0.6
-0.7
-0.8
-0.9
-1
-1.1
-1.2
-1.3
100
200
300
400
500
600
Temperature (°C)
Heating
Cooling

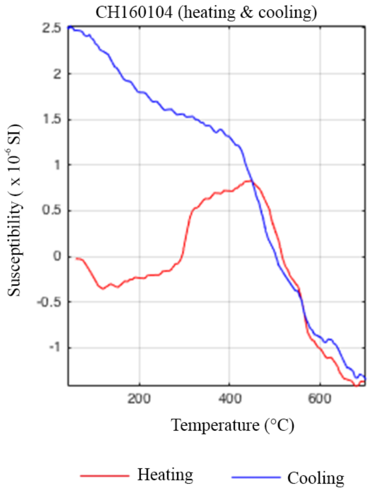
CH160104 (heating & cooling)
Susceptibility (x 10⁻⁶ SI)
2.5
2
1.5
1
0.5
0
-0.5
-1
200
400
600
Temperature (°C)
Heating
Cooling

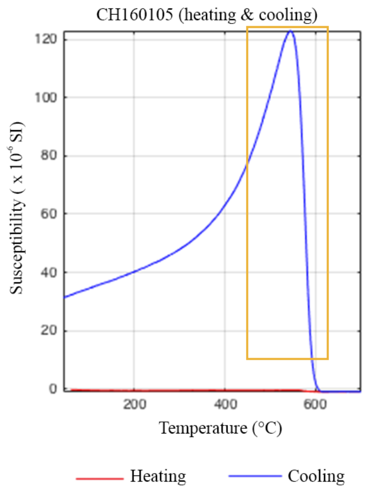
CH160105 (heating & cooling)
Susceptibility (x 10⁻⁶ SI)
120
100
80
60
40
20
0
200
400
600
Temperature (°C)
Heating
Cooling

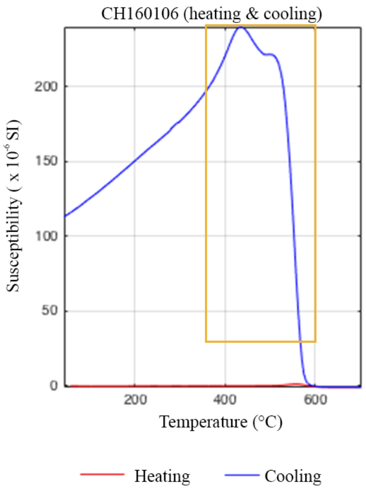
CH160106 (heating & cooling)
Susceptibility (x 10⁻⁶ SI)
200
150
100
50
0
200
400
600
Temperature (°C)
Heating
Cooling

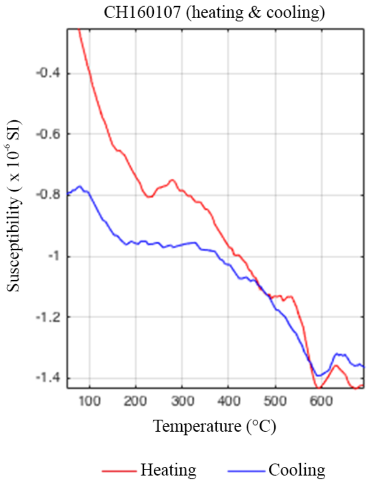
CH160107 (heating & cooling)
Susceptibility (x 10⁻⁶ SI)
-0.4
-0.6
-0.8
-1
-1.2
-1.4
100
200
300
400
500
600
Temperature (°C)
Heating
Cooling

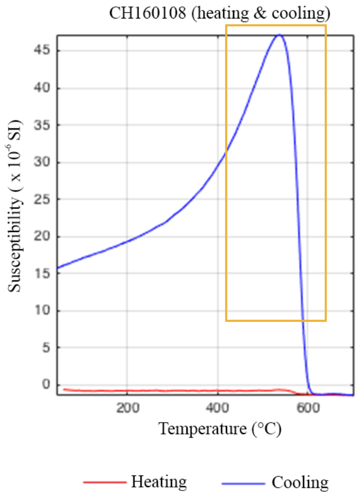
CH160108 (heating & cooling)
Susceptibility (x 10⁻⁶ SI)
45
40
35
30
25
20
15
10
5
0
200
400
600
Temperature (°C)
Heating
Cooling

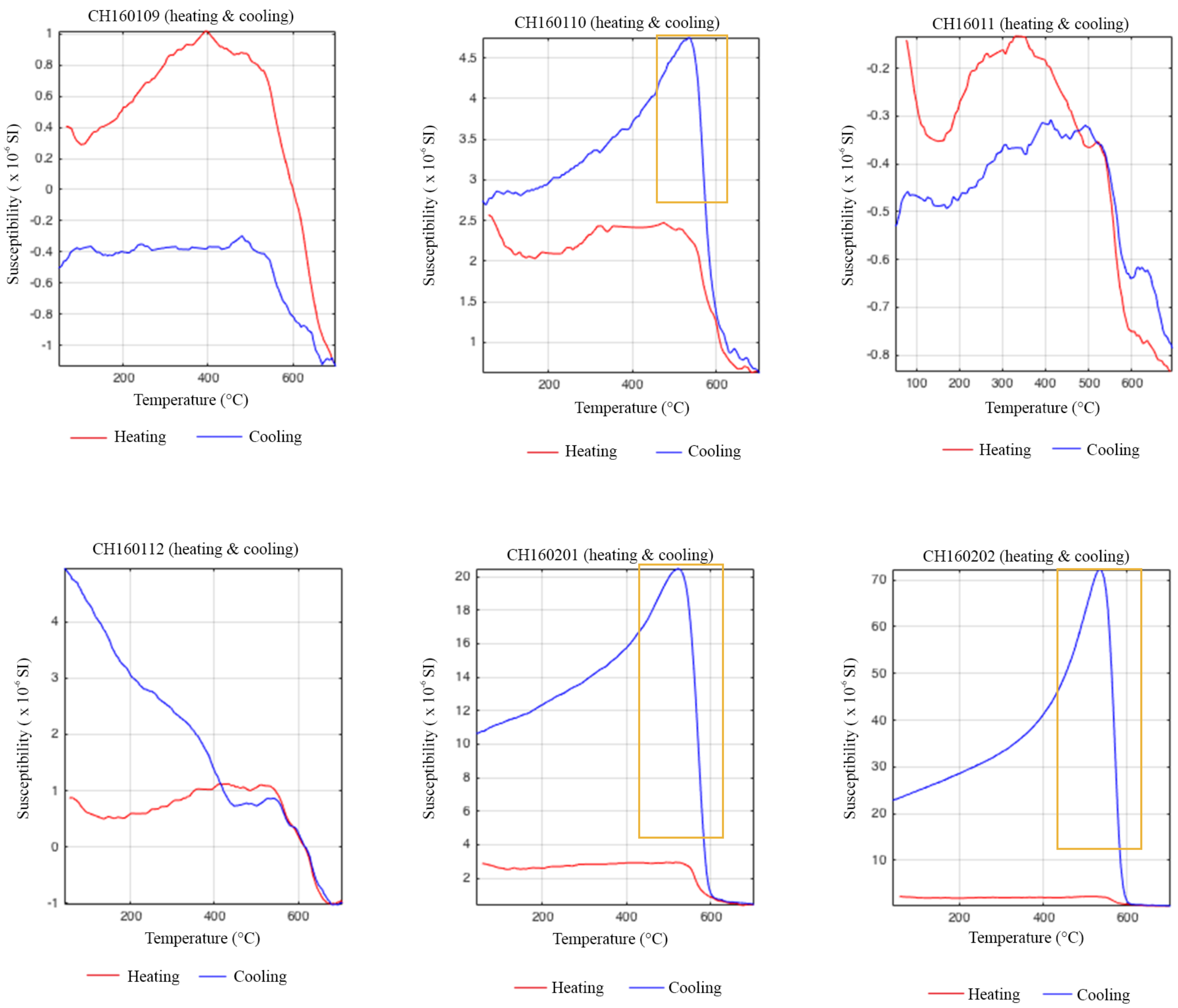

Figure 7: Data plots of the temperature dependent susceptibility

The heating curve is shown in red and the cooling curve is shown in blue. CH160101, CH160102, CH160102b, CH160105, CH160106, CH160108, CH160110, CH160201, and CH160202 exhibited magnetite. Hopkinson peaks (outlined with golden boxes) occurred during cooling for CH160101, CH160102, CH160102b, CH160105, CH160106, CH160108, CH160110, CH160201, and CH160202, which is suggestive of single domain magnetite grains. CH160101, CH160102, CH160102b, CH160105, CH160106, CH160108, CH160110, CH160201, and CH160202 displayed strong irreversibility between heating and cooling, demonstrated by the strong increase in susceptibility on cooling, likely reflective of the reduction of hematite to magnetite. CH160103, CH160107, CH160111, demonstrated the least amount of alteration during testing. CH160104 and CH160109 demonstrated moderate alteration from the heating and cooling procedure. Smoothing factors were used to reduce the amount of noise produced from taking the first derivative of the heating curves. A running mean 3-point smoothing factor was applied to CH160101, CH160102, CH160102b, CH160104, CH160105, CH160106, CH160108, CH160110, CH160112, CH160201, CH160202. A smoothing factor of 6 was applied to CH160109, a smoothing factor of 9 was applied to CH160107 and CH160111, and a smoothing factor of 12 was applied to CH160103.

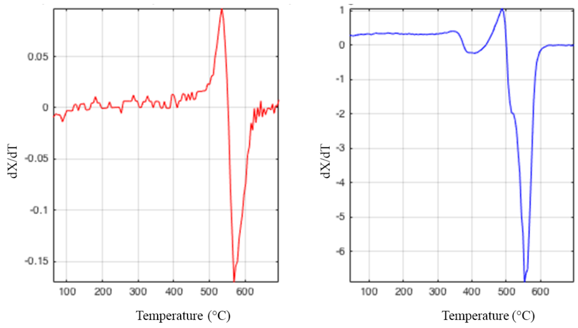

CH160101 First Derivative (heating & cooling)

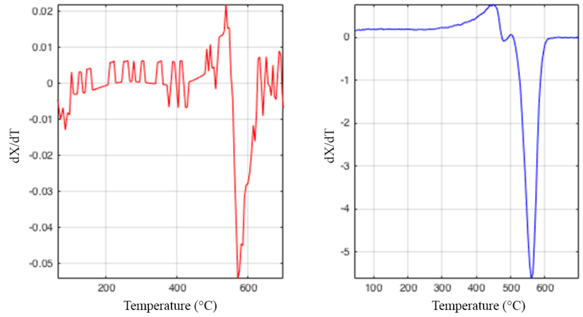

CH160102 First Derivative (heating & cooling)

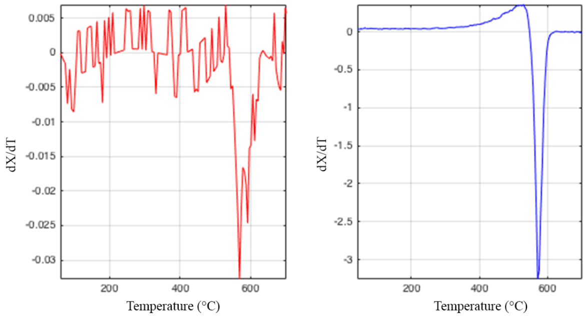

CH160102b First Derivative (heating & cooling)

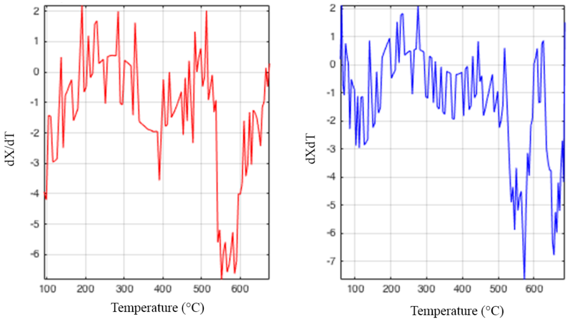

CH160103 First Derivative (heating and cooling)

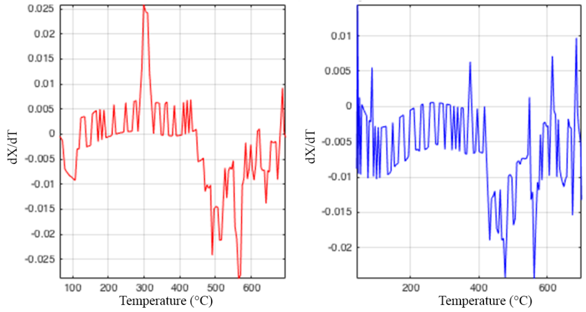

CH160104 First Derivative (heating & cooling)

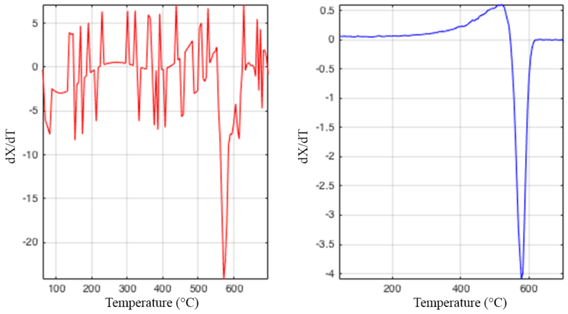

CH160105 First Derivative (heating & cooling)

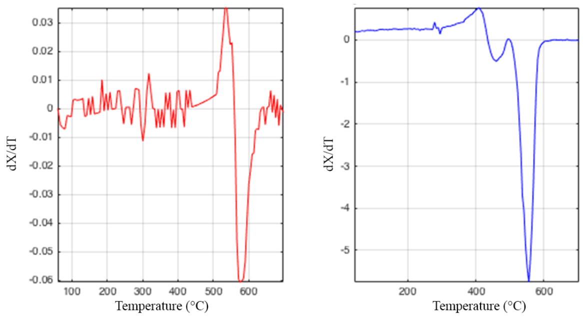

CH160106 First Derivative (heating & cooling)

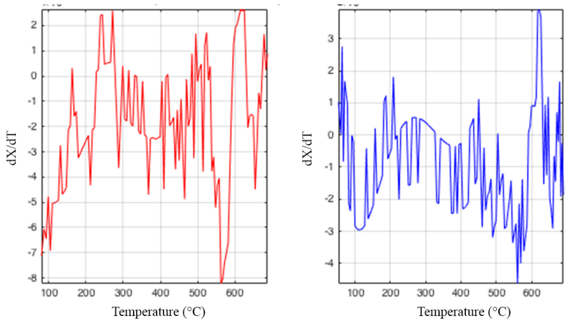

CH160107 First Derivative (heating & cooling)

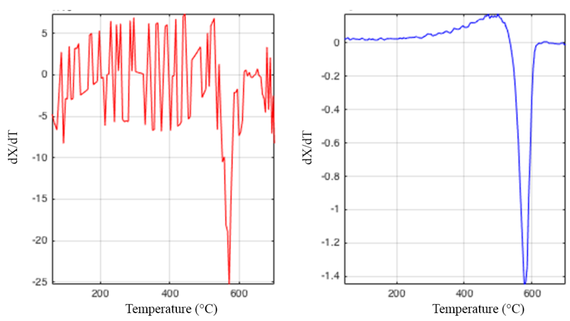

CH160108 First Derivative (heating & cooling)

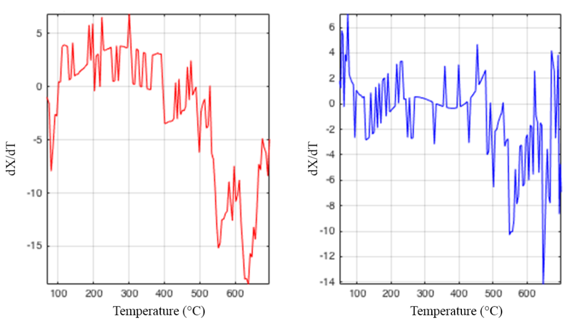

CH160109 First Derivative (heating & cooling)

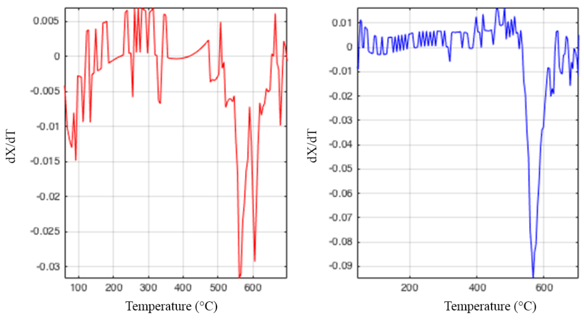

CH160110 First Derivative (heating & cooling)

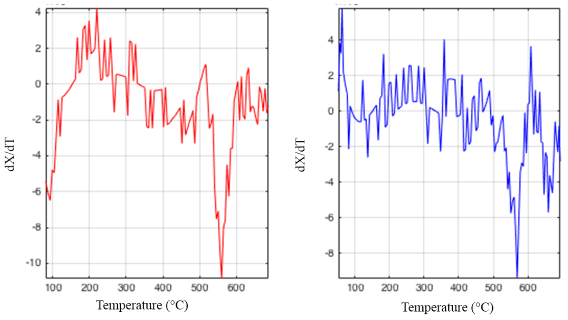

CH160111 First Derivative (heating & cooling)

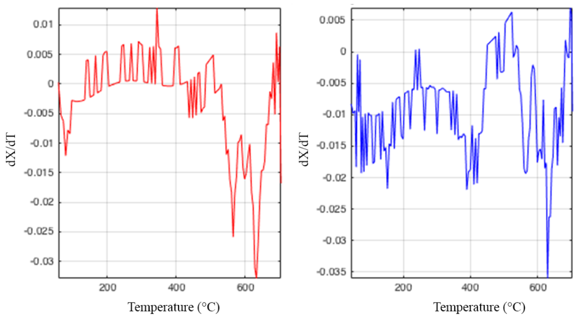

CH160112 First Derivative (heating & cooling)

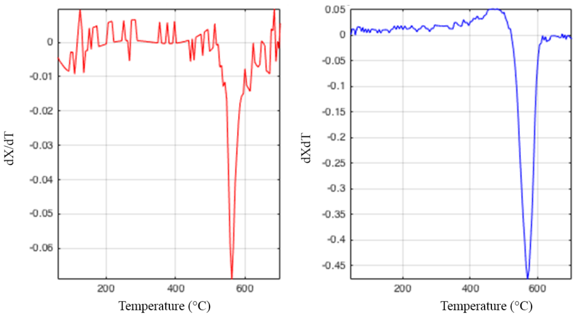

CH160201 First Derivative (heating & cooling)

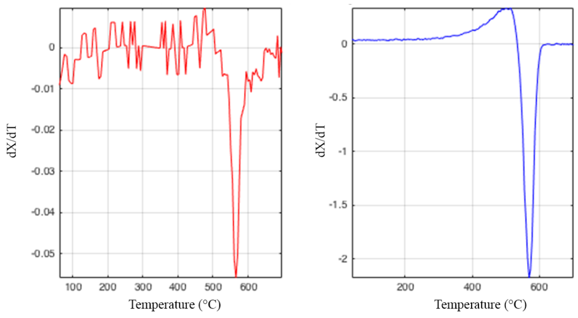

CH160202 First Derivative (heating & cooling)

Figure 8: First derivative of susceptibility as a function of temperature

The heating curve is shown in red and the cooling curve is shown in blue. The negative peaks represent the steepest slope of the heating and cooling curves from Figure 7. These peaks are used to identify the Curie temperature (Table 1).

4.4 IRM: Acquisition and Un-mixing

4.4.1 IRM Acquisition

None of the specimens from the first field season achieved saturation in a 1T field, reflective of a high-coercivity component such as hematite. The pilot specimens were the only ones subjected to the full step-acquisition process of magnetization described above in *Section 3.4.4*. Figure 9 features intensity that is normalized to IRM_{1T} to better compare magnetization acquisition behavior among specimens. Most specimens exhibited similar behavior (Fig. 9), except for Locality 2, which represented a slight divergence from the other samples with slightly lower coercivities. Locality 2 was composed of medium to coarse grain sand and was sampled

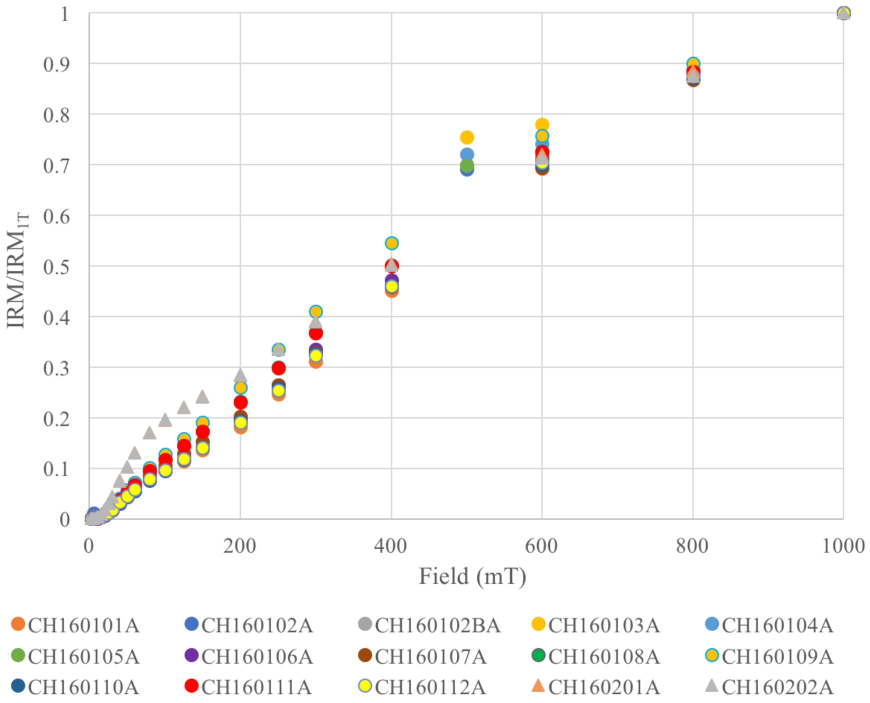

Figure 9: IRM acquisition of pilot samples, normalized to IRM_{1T}

IRM acquisition was consistent across all specimens for Locality 1. Specimens from Locality 2 demonstrated a slight variation of acquisition relative to Locality 1.

from friable rock that had endured heavy mechanical weathering directly on Lake Superior's shoreline.

4.4.2 IRM Un-mixing

The results of the IRM un-mixing are reported in terms of the peak coercivity of each skew-normal distribution (B_h), and the dispersion about that peak. Typically, a larger dispersion parameter (DP) indicates a wider range of magnetic grain sizes. To calculate the fractional contribution of each component to the IRM, the integrated area under each component is calculated. The observed contribution (OC) calculates the area under the measured data only. The extrapolated contribution (EC), extrapolates any non-saturated components to higher coercivities. The OCmean and ECmean values listed in Table 3 that were returned from the MAX Un-Mix program represent the mean distribution about the modeled approximation of the peak coercivity distribution (Maxbauer et al., 2016). In the present case, the EC is truer to the fractional amount of hematite present in the samples. All results revealed two primary magnetic components for each individual specimen (Table 3, Fig. 10). Locality 1: Component 1 had an average peak coercivity (B_h) of 1.71 (± 0.27) $\log_{10}$ mT (51.24 mT) and a DP of 0.27 (± 0.01) $\log_{10}$ mT (1.84 mT). Component 2 demonstrated significantly higher coercivity, with a mean B_h of 2.80 (± 0.03) $\log_{10}$ mT (630.55 mT) and an average DP of 0.38 (± 0.01) $\log_{10}$ mT (2.40 mT). Locality 2: Component 1 had an average B_h =1.72 (± 0.003) $\log_{10}$ mT (52.38 mT) and an average DP = 0.27 (± 0.005) $\log_{10}$ mT (1.86 mT). Component 2 had an average B_h = 2.85 (± 0.02) $\log_{10}$ mT (714.50 mT) and an average DP = 0.36 (± 0.01) $\log_{10}$ mT (2.30 mT).

Table 3: IRM un-mixing results

Specimen ID	**Bh_{C1} (log units)**	**DP_{C1} (log units)**	**EC_{C1} mean**	**Bh_{C2} (log units)**	**DP_{C2} (log units**	**EC_{C2} mean**
Locality 1						
CH160101A	1.70	0.25	0.06	2.81	0.36	0.94
CH160106A	1.70	0.25	0.06	2.79	0.37	0.94
CH160107A	1.71	0.27	0.06	2.85	0.39	0.94
CH160108A	1.71	0.28	0.08	2.79	0.39	0.92
CH160109A	1.69	0.26	0.07	2.73	0.40	0.93
CH160110A	1.71	0.27	0.06	2.82	0.38	0.94
CH160111A	1.73	0.28	0.08	2.79	0.39	0.92
CH160112A	1.72	0.26	0.06	2.80	0.36	0.94
Locality 2						
CH160201A	1.72	0.27	0.15	2.84	0.35	0.85
CH160202A	1.72	0.27	0.14	2.87	0.37	0.86

Table 3: Data headings contain subscript of C1 or C2 to denote Component 1 or 2, respectively. B_h represents the mean coercivity of the component, DP represents the dispersion parameter about the peak coercivity, and the ECmean represents the extrapolated component proportions since the samples were not fully saturated in a 1T field. Locality 1: Component 1 demonstrated a lower B_h on average (1.71 log units ± 0.01) than Component 2 (2.80 log units ± 0.03) as well as an overall lower DP (Component 1 (0.27 log units ± 0.01)); Component 2 (0.38 log units ± 0.01). The average coercivity of Component 1 was 51.2 mT, suggestive of magnetite and the coercivity of Component 2 was 630.6 mT, suggestive of hematite. Locality 2: Component 1 B_h average 1.72 ± 0.003, DP average 0.27 ± 0.005, coercivity 52.4 mT. Component 2 Bh average 2.85 ± 0.02, DP average 0.36 ± 0.01, coercivity 714.4 mT.

CH160101A

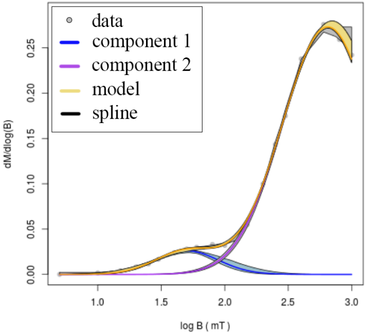

CH160106A

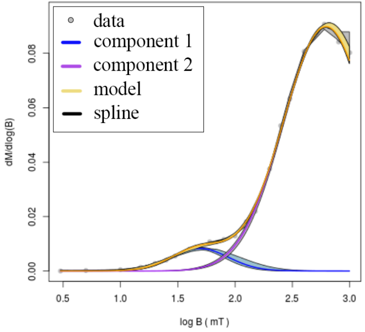

CH160107A

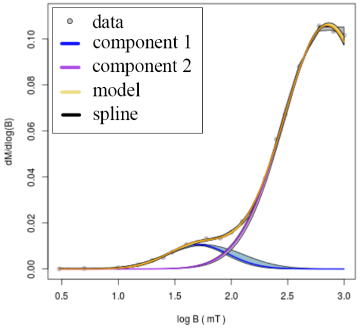

CH160108A

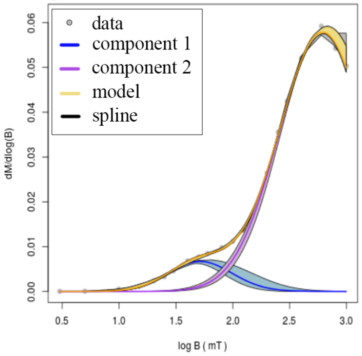

CH160109A

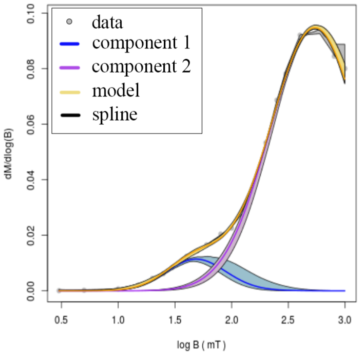

CH160110A

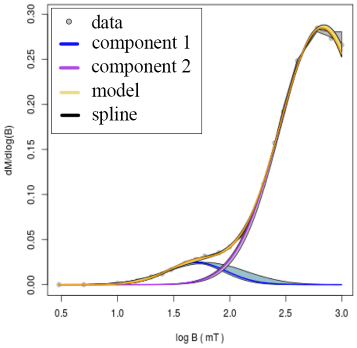

CH160111A

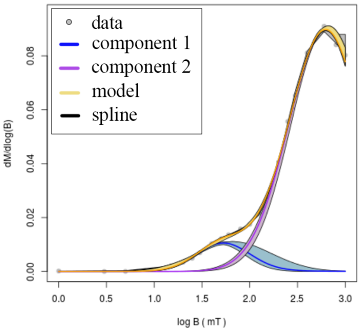

CH160112A

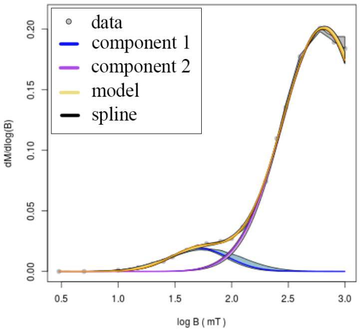

CH160201A

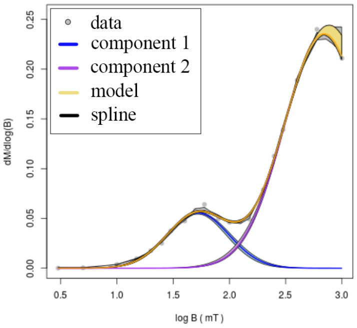

CH160202A

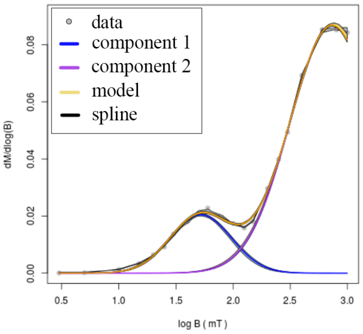

Figure 10: IRM un-mixing results

These plots represent the first derivative of IRM acquisition that was obtained through 20 steps from 0-1 T. The first derivative was taken using the MAX un-mix web application. The curves were consistently representative of two magnetic components, one of low coercivity (Locality 1, $C1_{avg}$ = 51.3 mT; Locality 2, $C1_{avg}$ = 52.4 mT) and one of high coercivity (Locality 1, $C2_{avg}$ = 631.0 mT; Locality 2, $C2_{avg}$ = 708.0 mT).

The Locality 1 average contributions of the hard and soft component were 90.63% ± 1.09% and 9.37% ± 1.09%, respectively. The Locality 2 average contributions were 78.79% ± 0.29% of the hard component and 21.21% ± 0.29% of the soft component. Although the IRM un-mixing data give a detailed picture of coercivity distributions in the sample, the data collection process is lengthy and it was unfeasible to collect this data on a much larger sample set. Subsequent samples from the second field season were not subjected to this detailed IRM un-mixing process. Instead, the S-ratio, hard- and soft-IRM parameters seem to provide similar information on abundance and relative proportions of hard and soft minerals (Fig. 11). Although the correlations are imperfect, they generally follow the expected trends. For example, the hard-IRM

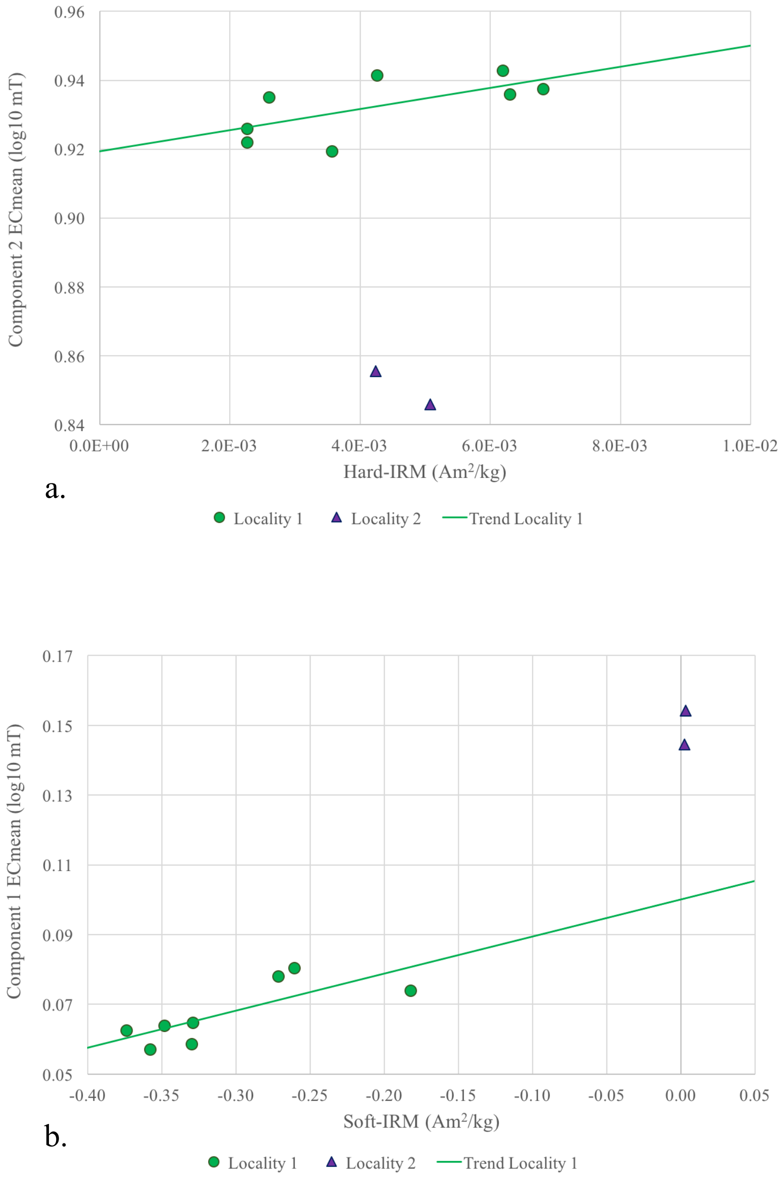

Figure 11: Correlation of components relative to extrapolated contribution mean

Locality 1: (a.) The Hard-IRM correlates positively with the extrapolated contribution of Component 2 which was determined by the IRM un-mixing curves. (b.) The Soft-IRM correlates positively with the extrapolated contribution from Component 1. Locality 2 for both comparisons represent their own trend.

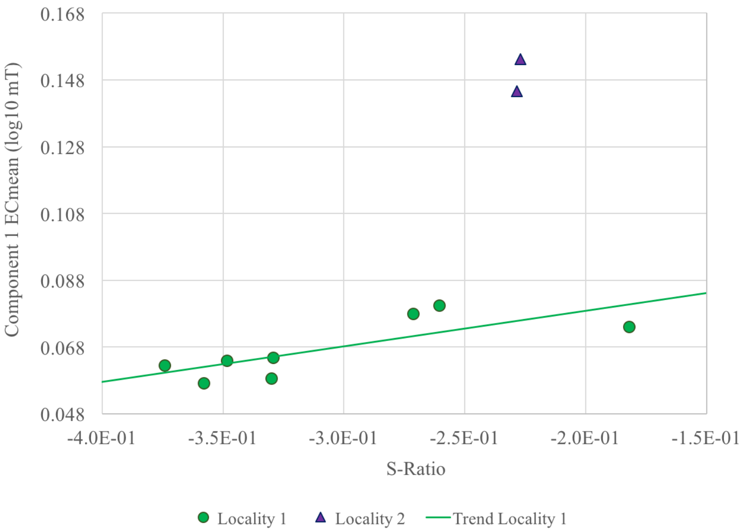

Figure 12: Correlation of S-ratio to extrapolated contribution from component 1

The S-ratio correlates positively with the extrapolated contribution of Component 1.

compared with the extrapolated contribution from the hard mineral (Component 2), as determined by the IRM-un-mixing process, demonstrated a positive trend (Fig. 11a). The soft-IRM also featured a positive trend when compared relative to the extrapolated contribution of the soft mineral (Component 1) (Fig. 11b). The S-ratio average was -0.33 ± -0.08 and was found to vary from -0.69 to -0.15. These consistently negative S-ratio values support the significant presence of hard minerals, such as hematite, that was inferred from the inability of the samples to reach full saturation in a 1T field. The positive correlation of the S-ratio to the extrapolated contribution of the soft mineral (Component 1) corroborated these observations since as the S-ratio became less negative there was a greater contribution from the soft minerals (Fig. 12). The Hard-IRM average was 4.13 x 10^{-3} Am^2/kg ± 0.001, the data varied from 3.02 x 10^{-3} Am^2/kg to 6.81 x 10^{-3} Am^2/kg that again suggested that the hematite contribution is greater than that of magnetite since in both instances the hard-IRM was greater than the soft-IRM. The soft-IRM average was 2.10 x 10^{-3} Am2/kg ± 0.001. The SIRM average was 6.23 x 10^{-3} Am^2/kg ± 0.002.

The hard- and soft-IRM were compared with overall bulk susceptibility. The hard-IRM demonstrated a positive, linear trend and the soft-IRM did not display a clear correlation (Fig. 13). Overall, susceptibility seems to correlate with the magnetic remanence associated with hematite. This correlation is important because it would suggest that the hematite and not the magnetite controls the outcrop susceptibility variations.

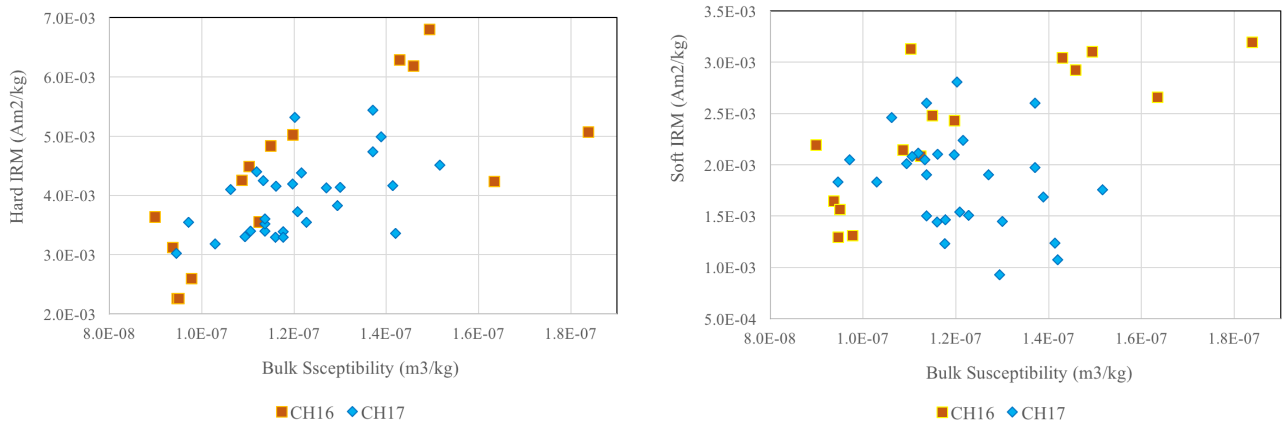

Figure 13: Hard and soft component correlation with overall bulk susceptibility

The preliminary samples (from 2016 field season) demonstrated a positive linear trend between bulk susceptibility and the soft IRM component, however subsequent data (from 2017 field seasons) did not follow this correlation. Ultimately both data sets demonstrated a positive linear trend between the hard-IRM (Component 2) and bulk susceptibility.

4.5 Anisotropy of Magnetic Susceptibility (AMS)

4.5.1 Anisotropy Shape

Measured AMS eigenvalues of the pilot samples were used to determine the overall degree of anisotropy (P) by τ_1/τ_3, foliation (F) by τ_2/τ_3, and lineation (L) by τ_1/τ_2, at the specimen level. The overall P was determined to be low with an average of 1.016, the average of F was 1.006, and the average of L was 1.010. When L and F are plotted on a Flinn diagram (Fig. 14), most data fall above the 1-1 line of increasing anisotropy indicative of a predominantly prolate shape. Data that fall below the 1-1 line are representative of a dominantly oblate shape (Flinn, 1982). The only bedding types that seemed to demonstrate a consistent shape are rippled bed-forms which all fall within the range of prolate to triaxial shape, fine laminations that are very nearly isotropic, and mud-cracks which plot above the line of increasing anisotropy as a prolate shape.

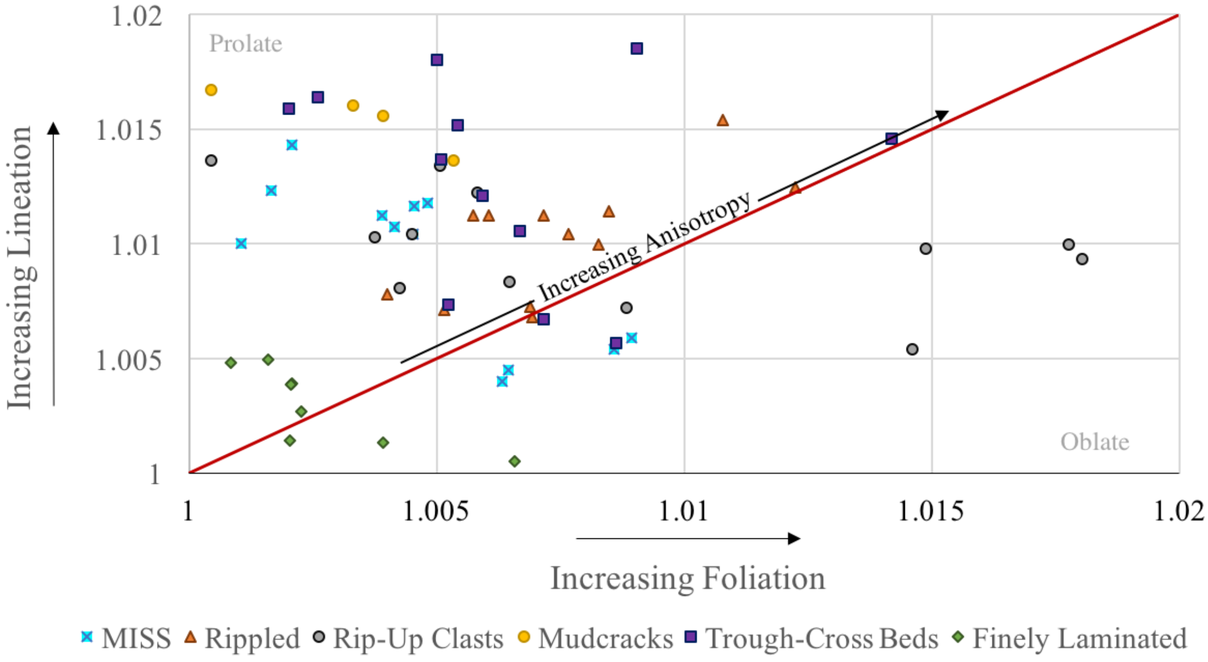

Figure 14: Flinn diagram

A prolate shape is plotted above the line of increasing anisotropy, while oblate shapes are plotted below. Data that plots closest to the 1-1 line are triaxial. Although most bedding types did not exhibit a distinct trend between bed-form and shape anisotropy, rippled bedding ranged between triaxial and prolate shape, fine laminations were primarily isotropic, and mud-cracks were prolate.

4.5.2 Anisotropy orientation

Because the CHC bedding has a regional tilt of approximately 21° towards the N-NE, the resulting AMS data were corrected for tilt. The AMS data, at the site level (Locality 1), place the minimum axes (**V**$_3$) as clustered and smeared across the vertical stereoplot axis, trending mostly within the NW quadrant. The maximum axes ($\mathbf{V}_1$) are mostly clustered within the SW and NE quadrants of the stereoplot within the horizontal plane (Fig. 15). Under moderate flow conditions, current direction is typically determined from the sense of imbrication of the $\mathbf{V_3}$ axes. However, the smearing of the $\mathbf{V_3}$ axes is not entirely in support of this method of interpretation and rather suggests that flow direction may have been turbulent and was likely moving perpendicular to the $\mathbf{V_1}$ axes (Tauxe, 2016). Such an interpretation would suggest that a paleocurrent was moving either towards the NW or SE, with preference towards the NW based on the clustering of the $\mathbf{V}_3$ axes in the NW quadrant. Previous paleocurrent measurements near Union Bay that were based on pebble imbrication, by Wolf and Huber (1973), provide a NE to NW paleocurrent direction. Paleocurrent measurements based on bedding features within the Union Bay outcrops conducted by University of Wisconsin-Milwaukee graduate student, Jenny Ulbricht, depicts a NW paleo-current direction (personal communication, 2018), consistent with the AMS results.

The AMS for CH16 pilot samples from Locality 2 (Fig. 16) was less well defined than that for Locality 1. The data do not seem to indicate any discernable geographic trend. This is likely related to the small number of samples and an overall low degree of anisotropy, which precludes making interpretations about the method and flow direction of deposition.

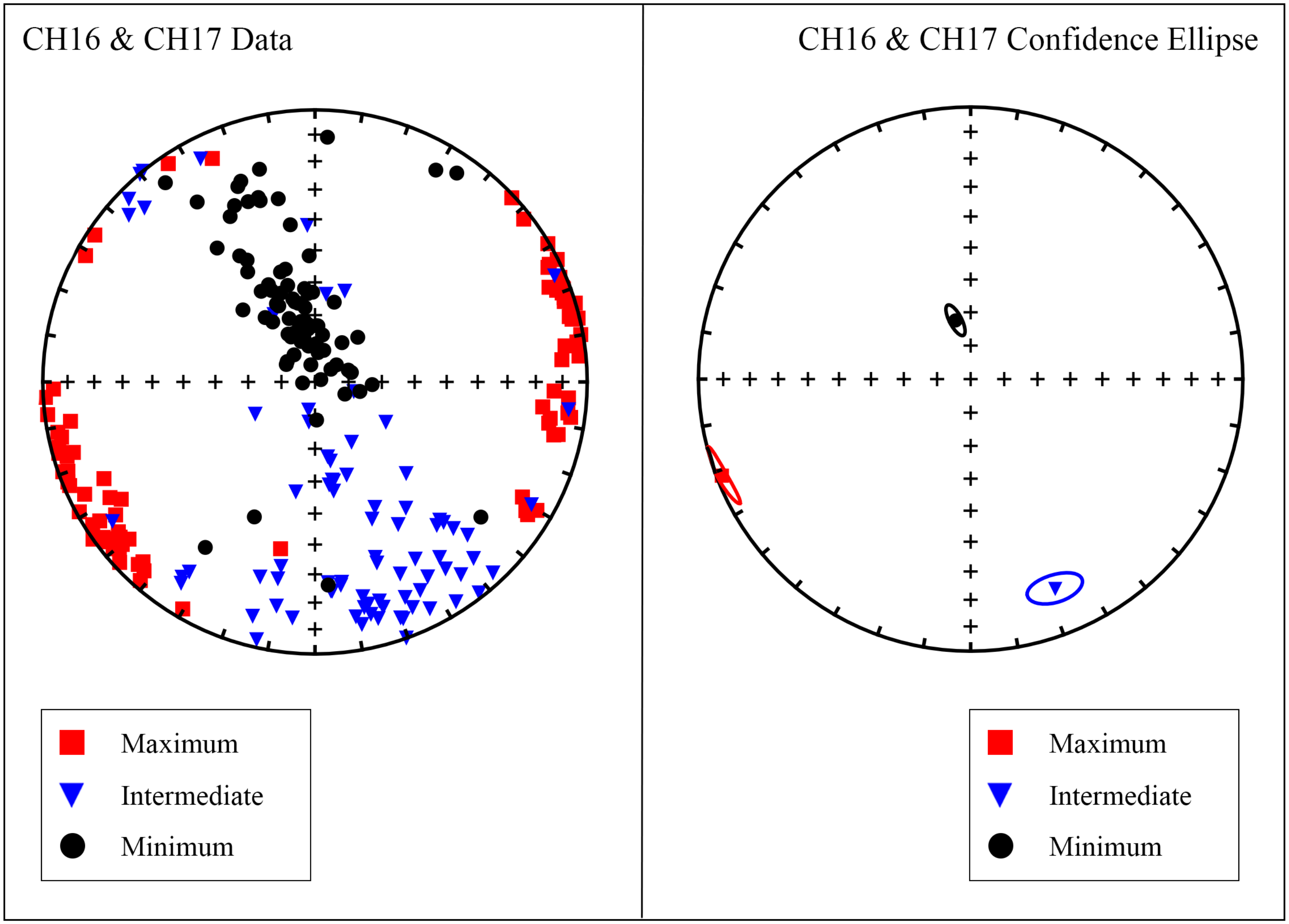

Figure 15: Locality 1, CH16 & CH17 AMS data and data bootstrap

The data are plotted in the lower hemisphere. The grain sizes are primarily prolate (Fig. 6 & 14). The smearing of the $\mathbf{V}_3$ and $\mathbf{V}_2$ axes across the center of the plot is suggestive of a depositional environment of fast moving or turbulent flow. If this is the case, then $\mathbf{V}_1$ should be oriented perpendicular to flow. The paleo-flow would be directed towards the NW, headed in the direction of the central axis of the Keweenawan trough of the MCR.

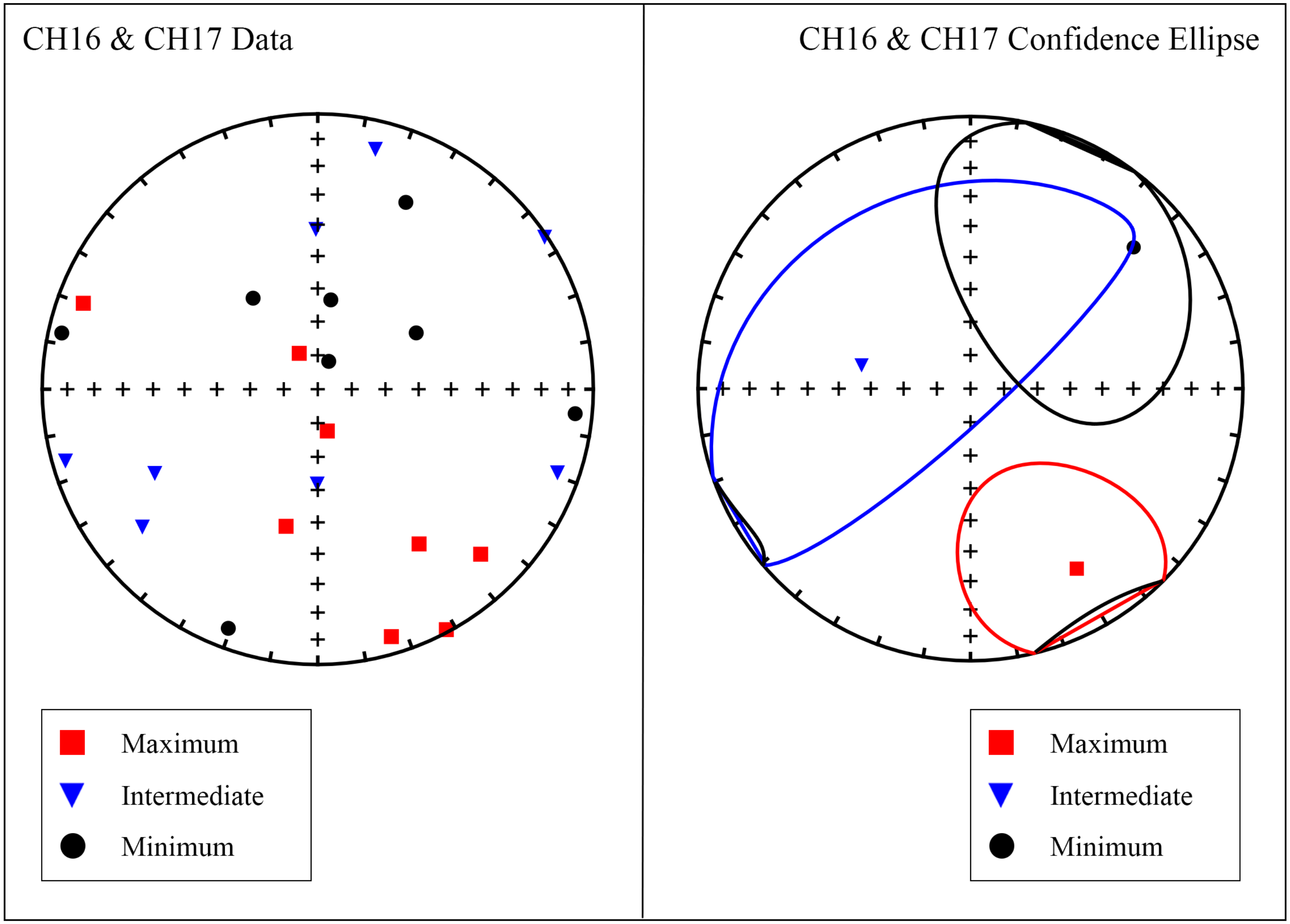

Figure 16: Locality 2, CH16 & CH17 AMS data and data bootstrap

The data are plotted in the lower hemisphere. Due to the low sample number collected at this locality, the data is inconclusive.

4.6 Stratigraphic Susceptibility

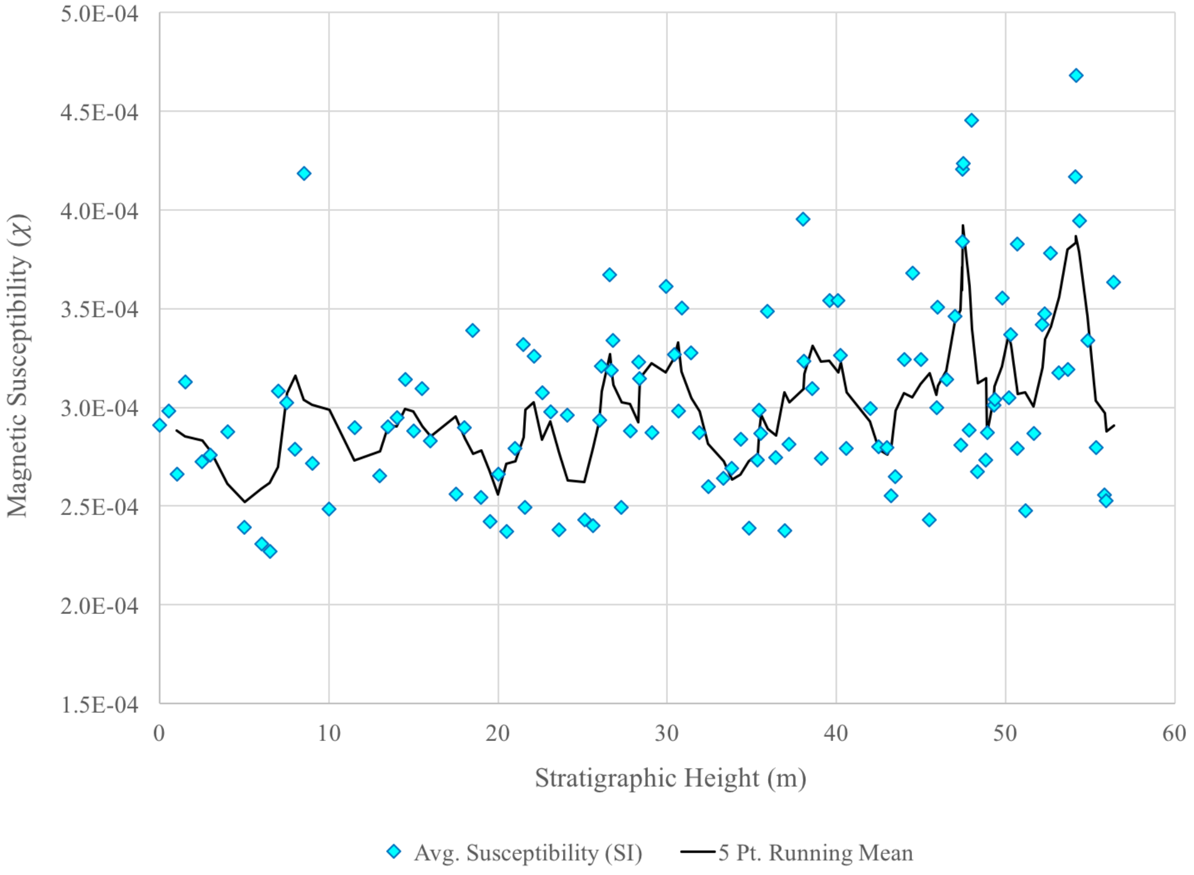

Figure 17: Magnetic susceptibility increases up-section

The boat launch at Union Bay State Park is representative of 0m. Moving up section, susceptibility measurements were taken approximately every 0.47m for a total stratigraphic height of 56.4m.

The magnetic susceptibility values range from 2.27×10^{-4} to 4.68×10^{-4} SI, and in general, susceptibility increases up section (Fig. 17). Application of a simple 5-point running mean seems to highlight some periodicity in the data. To investigate possible cyclicity in the data further, we can examine the spectral analysis (Fig. 18). Only one peak with a frequency of 0.48 m^{-1} (significance every 2.08 m) was statistically distinct from the background robust red noise estimation with >99% confidence. Additionally, two broader peaks of lower confidence were present in the spectral output. The broadest peak ranged between frequencies of 0.40 to 0.56 m^{-1} (significance every 1.79 m - 2.5 m), and represents peaks statistically distinct with >90% confidence. A peak with >80% confidence represents an approximate frequency of 0.17 m^{-1} (significance every 5.88 m).

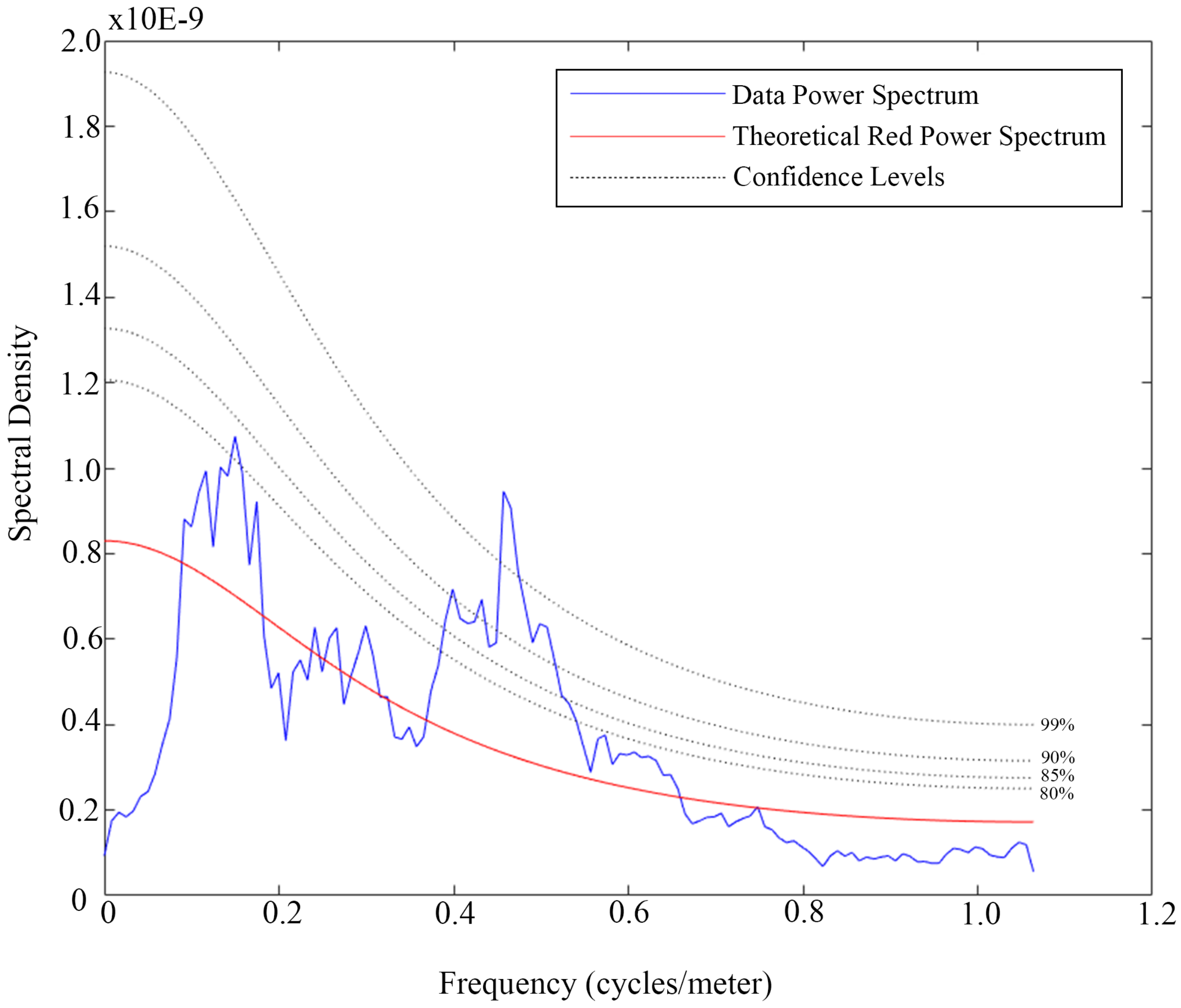

Figure 18: Stratigraphic susceptibility power spectrum

The data power spectrum (blue curve) is the result of the spectral analysis of magnetic susceptibility data collected in the field. From the data power spectrum, the robust red noise (red curve) was estimated using the Monte Carlo simulation. Peaks above the red noise curve are distinct from background noise. However, peaks above the 80%, 85%, 90%, and 99% confidence limit (black dashed lines) are representative of significant peaks not related to background noise.

4.7 Outcrop Susceptibility Variation Grids

4.7.1 Grid 1

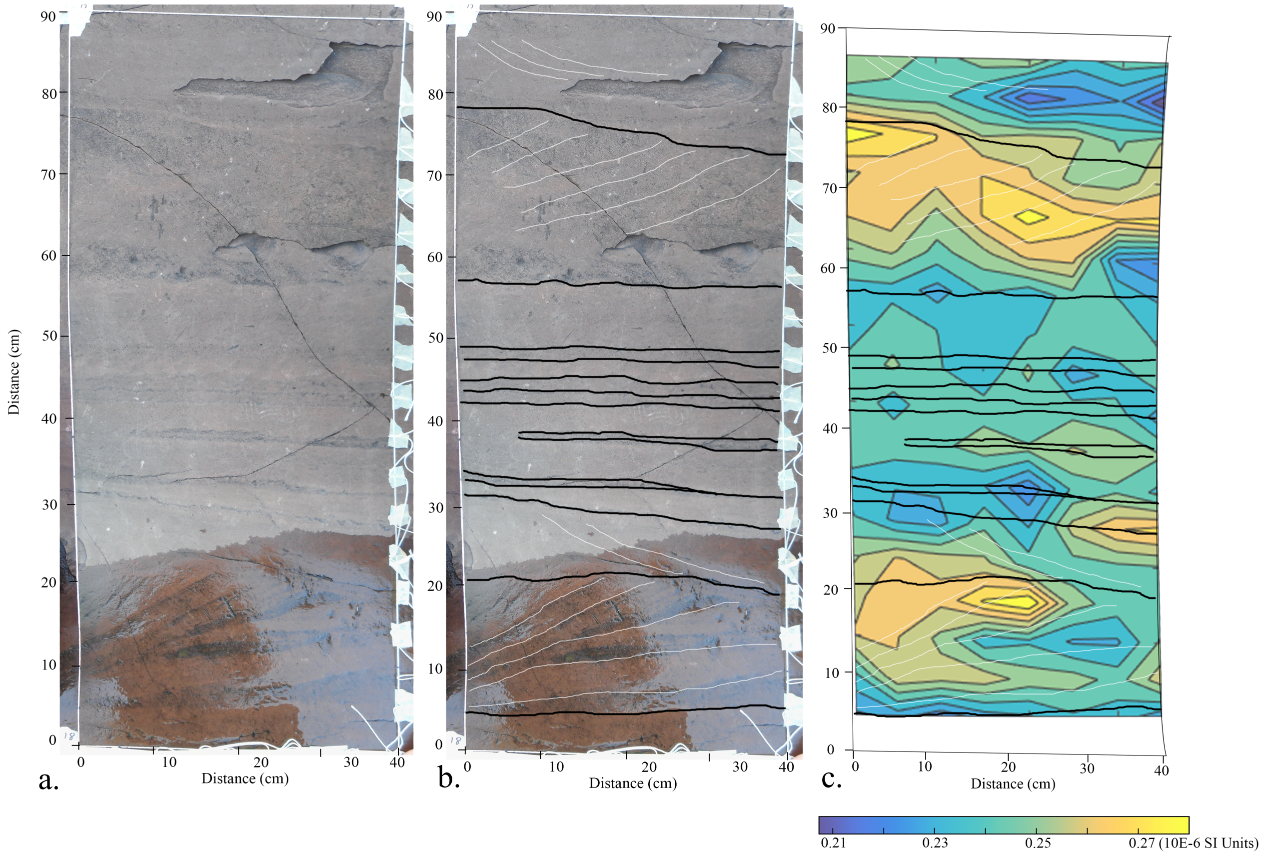

Figure 19: Grid 1

(a.) Grid 1 without any annotation. (b.) Grid 1 with bedding contacts drawn in with black lines, bedding features are depicted with thin white lines. (c.) Grid 1 magnetic susceptibility map and the annotations of depositional features. The susceptibility strength (SI units) is denoted by color. Warm colors are indicative of high susceptibility while cool colors are representative of low susceptibility. Poor contact in the upper right corner demonstrated extremely low susceptibility measurements. Highest susceptibility measurements were associated with the lowest erosion bounded depositional unit of foresets and the upper erosion bounded unit of lower medium-grained sandstone. The foresets near the base of the grid demonstrated grain size variability from upper fine- to lower medium-grains and is bounded by fine-grains. The upper erosional bounded unit is composed of lower medium-grains and is bounded by fine-grains as well.

The purpose of both outcrop susceptibility grids was to demonstrate the amount of magnetic variability at a spatial scale smaller than the ~0.5 m spacing that was used for the entire stratigraphic section. The first grid is a 90 x 40 cm section featuring multiple sediment packages (Fig. 19). This grid is located below a continuous erosional surface and contains a section of well sorted, fine- to medium-grained, cross-bedded, sublitharenite sandstone. The base of the grid begins with dipping foresets, approximately 20 cm in height, of upper fine- to lower medium-grain sandstone. The top of these foresets are truncated by a minor erosional surface. Above the erosional contact exists a trend of multiple, fining-upward packages of primarily horizontal laminations alternating from upper fine- to lower medium-grained sandstone. Eventually these laminations are truncated by an erosional contact and the overlying package transitions to an approximately 20 cm thick layer of lower medium-grained sandstone. This thicker package of lower medium-grained sandstone is overlain by another package of fine-grained sandstone with an erosional contact between the two sediment packages.

The overall magnetic variability demonstrated within this grid was smaller than the range for the entire stratigraphic section (Fig. 17). The magnetic susceptibility ranged from 2.08 x 10^{-4} to 2.85 x 10^{-4} SI units. Occasional areas of small cavities or cracks related to weathering and erosion on the outcrop surface prevented flush contact between the outcrop and the KT-10 Magnetic Susceptibility Meter that seemed to correlate with lower susceptibility measurements. Higher susceptibility exists near the base of the grid, about 5 cm from the bottom to approximately 25 cm. These higher susceptibility measurements do not extend across the entire width of the grid, but end about 25 cm across the extent of the grid, when moving from left to right. Another area of higher susceptibility exists horizontally across the grid at a lateral height approximately 60 to 80 cm from the bottom. This higher susceptibility extends across the entire 40 cm width of the grid. The higher susceptibility near the base of the grid is associated with the approximate location of the steeply dipping foresets with greater grain size variation, while the higher susceptibility near the top of the grid is associated with the thicker band of lower medium-grained sandstone.

4.7.2 Grid 2

Grid 2 covers a greater surface area than that of the first grid. Grid 2 outlines a section of cross-beds of a well-sorted, fine- to lower medium-grained, cross-bedded, sublitharenite sandstone section. The bottom right side of Grid 2 exhibits steeply dipping, tangential foresets of trough cross-bedding (Fig. 20 & 21). This basal package has a top and bottom that are both truncated by erosional surfaces. Most of the section within the grid is similar to the base. Moving upwards vertically, the lower to middle portion of the grid is comprised of multiple packages consisting of small depositional events. Approximately 1 m from the top of the grid there is a shift in the mechanism of deposition to larger cross-beds that have a base marked by a mostly continuous, erosional surface that extends the length of the grid. Approximately 45 cm from the top of the grid a second continuous erosional surface occurs. This surface truncates the tops of the larger cross beds below it, while above this surface exists a second package of large cross beds. These relatively large, erosional bounded cross beds near the top of this grid are interpreted as eolian dunes as they are well-sorted, predominantly fine-grained sandstone, and they are both sharply bounded by erosional tops and sharp lower contacts (Mountney, 2006; Langford and Chan, 1989). All cross beds within this grid represent an overall fining upwards succession.

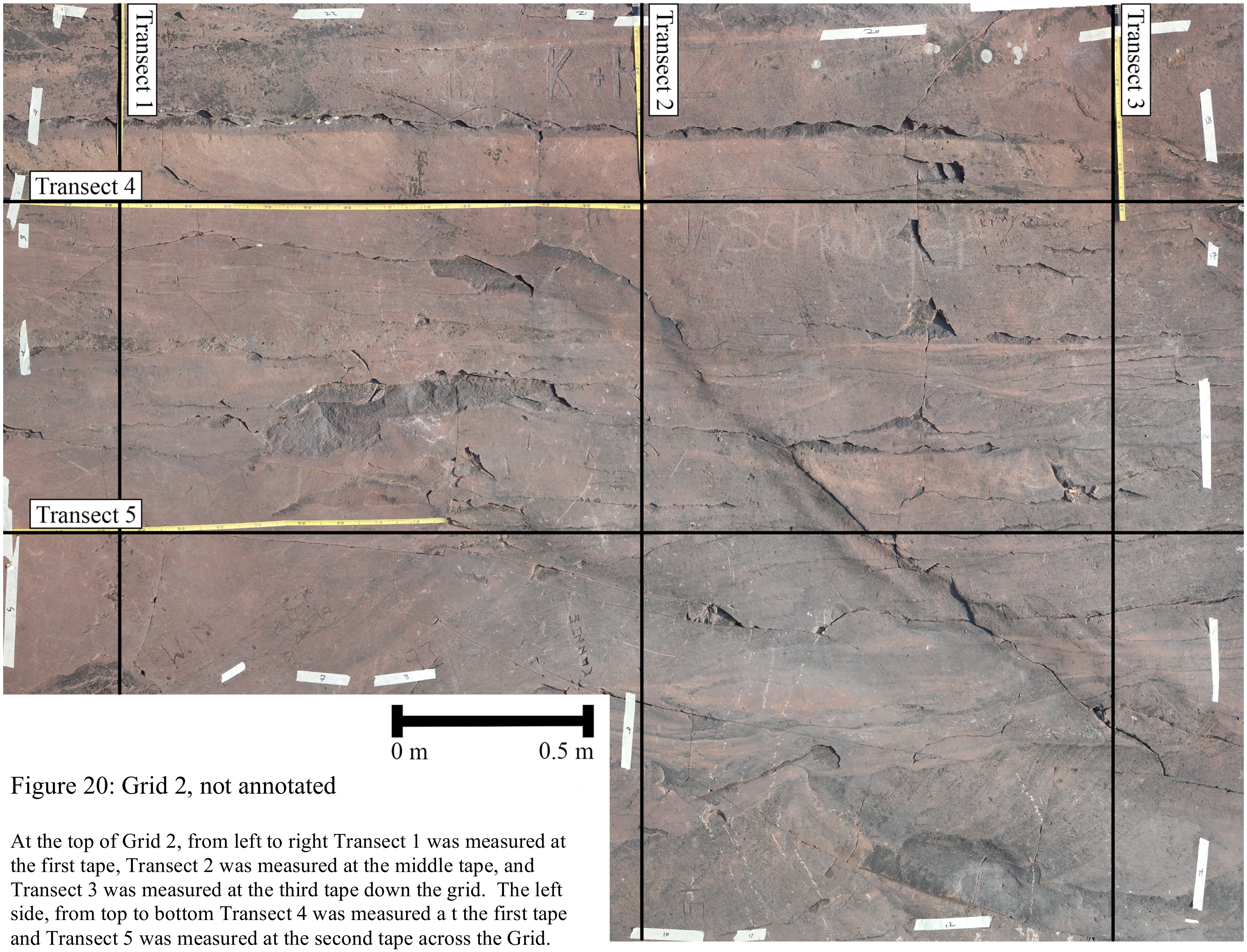

Figure 20: Grid 2, not annotated

At the top of Grid 2, from left to right Transect 1 was measured at the first tape, Transect 2 was measured at the middle tape, and Transect 3 was measured at the third tape down the grid. The left side, from top to bottom Transect 4 was measured a t the first tape and Transect 5 was measured at the second tape across the Grid.

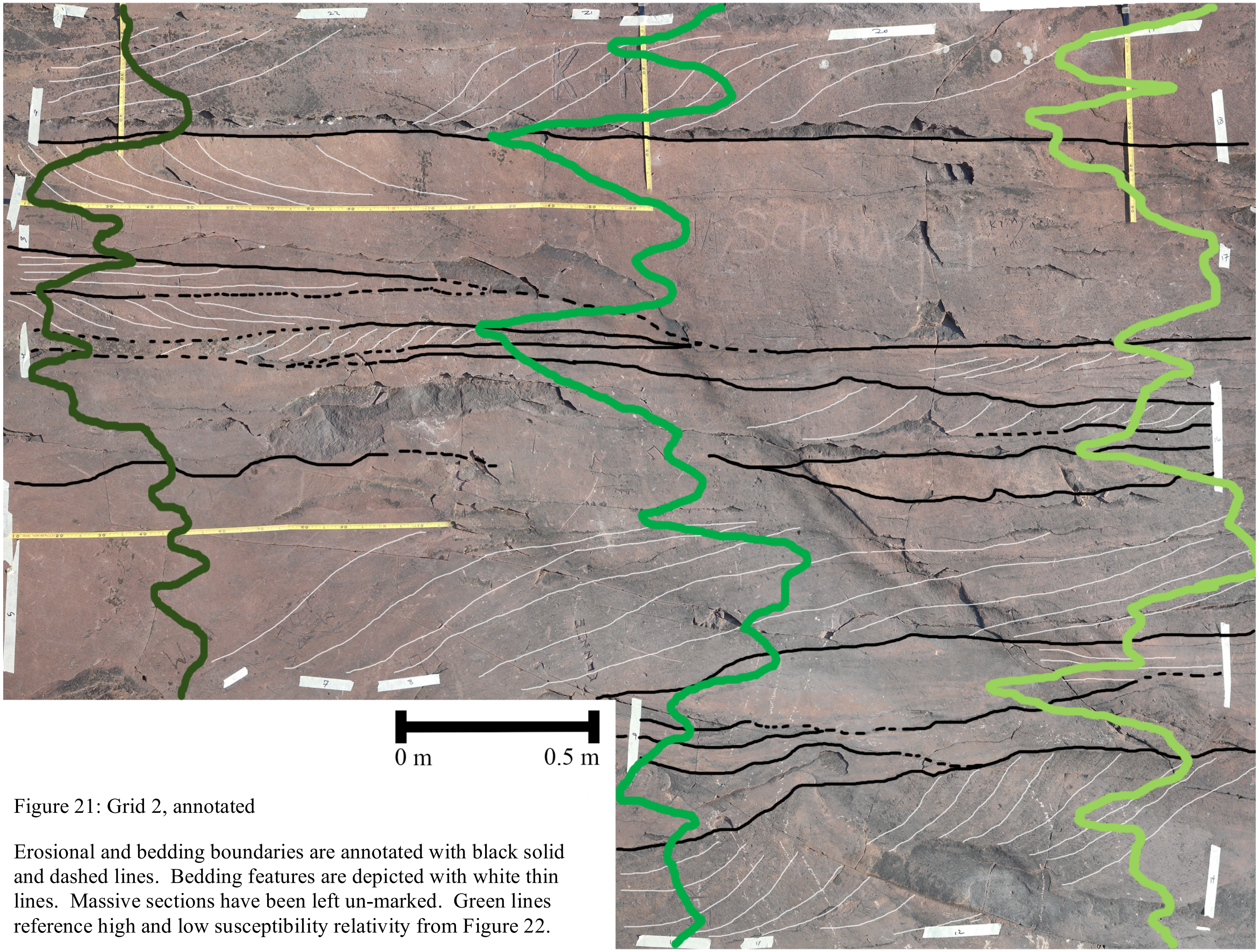

Figure 21: Grid 2, annotated

Erosional and bedding boundaries are annotated with black solid and dashed lines. Bedding features are depicted with white thin lines. Massive sections have been left un-marked. Green lines reference high and low susceptibility relativity from Figure 22.

The magnetic susceptibility of Grid 2 was not measured as comprehensively as was done for Grid 1, rather three vertical and two horizontal transects were measured to estimate lateral and vertical variability within this section of the outcrop (Fig. 22). The magnetic susceptibility varies from 1.86 x 10^{-4} to 3.18 x 10^{-4} SI units vertically and 2.33 x10^{-4} to 3.30 x 10^{-4} SI units horizontally. The lowest values in this grid were influenced by poor contact between the susceptibility meter and the uneven surfaces of the outcrop. This larger grid demonstrates a wider range of susceptibility than was detected in Grid 1.

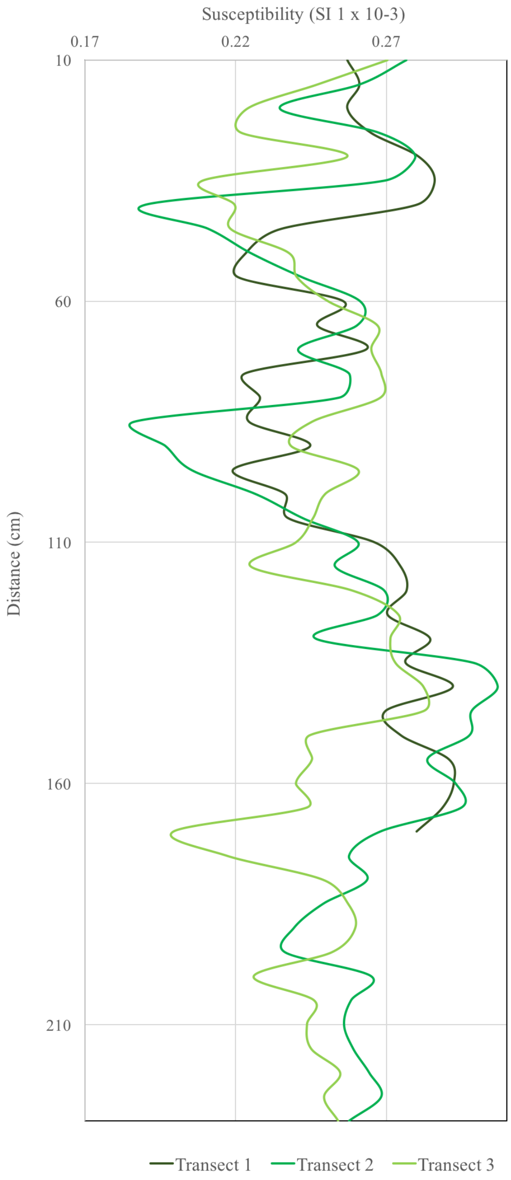

Figure 22: Comparison of transect susceptibility measurements from Grid 2

The vertical transect measurements are denoted by various shades of green lines and the horizontal transects are denoted by various shades of blue lines. The horizontal transects are representative of overall greater susceptibility relative to the vertical transects. The vertical transects are more consistent with one another relative to the horizontal transects.

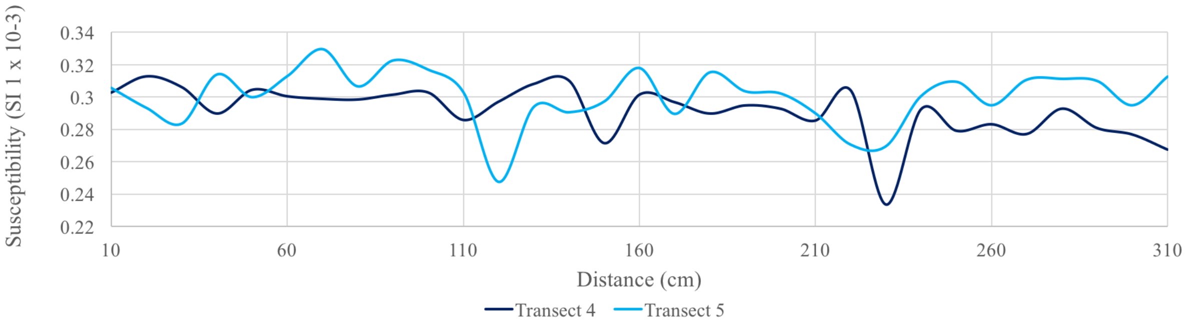

However, the observed range of susceptibility for Grid 2 is still smaller than what was measured throughout the entire section. The vertical transects show similar susceptibility trends, suggesting roughly consistent along-bedding magnetic variability. This is suggestive of steady deposition longitudinally, over a scale of 3.10 m. Meanwhile the horizontal transects are less similar to one another. In general, the susceptibility lows seem to correspond to either erosional, bedding boundaries, or color changes while susceptibility highs existed between these boundaries (Fig. 21 & 22).

CHAPTER 5. DISCUSSION

5.1 General Observations

Magnetic characteristics identified in this study support the presence of two magnetic components and are overall consistent with the findings of Elmore and van der Voo (1982). The IRM un-mixing results demonstrated two distinct magnetic components and temperature dependent susceptibility corroborated these observations. The first component had an average coercivity of 51.24 mT and T_C ranging from 560-590 ºC which is near the T_C of pure magnetite (580ºC). The second component had an average coercivity of 630.55 mT and T_C ranging from 630-680 ºC which is near the T_C of hematite (675ºC). Coercivities of the two CHC components can be compared with average magnetic coercivities identified by Egli (2004). Egli's (2004) modeled coercivities are based on IRM un-mixing data and include detrital magnetite (B_h=28.84 mT, DP=2.29 mT), low-coercivity magneto-fossils (B_h=43.65 mT, DP=1.55 mT), hematite (B_h=199.53 mT, DP=1.86 mT), and goethite (B_h=1995.26 mT, DP=1.78 mT). Our low-coercivity component, interpreted to be detrital magnetite, has higher coercivity (B_h=51.24 mT, DP=1.84 mT) relative to the detrital magnetite component of Egli (2004) (B_h=28.84 mT, DP=2.29 mT). This suggests that our magnetite grain size is finer than that of typical detrital magnetite, but likely reflects a volcanic source for these sediments which contain SD-PSD (titano-)magnetite. Our high-coercivity component also has relatively higher coercivity (B_h=630.55 mT, DP=2.40 mT) relative to the hematite component observed by Egli (2004) (B_h=199.53 mT, DP=1.86 mT). Again, this is suggestive that our hematite component is predominantly fine-grained.

5.2 Evaluation of Susceptibility as a Deposition Signal

Hematite undoubtedly dominates the remanence, and Elmore and van der Voo (1982) demonstrate that the hematite remanence direction is clearly younger than the magnetite direction, consistent with authigenic hematite. Since the susceptibility signal is also dominated by hematite, the cyclical variations we observe may be unrelated to depositional processes or conditions considering that Elmore and van der Voo (1982) observed both detrital and authigenic hematite at Union Bay. A secondary signal produced from the formation of completely new magnetic minerals could obscure the magnetic variations related to the original depositional signal.

There are several arguments to be made, however, that the susceptibility reflects a depositional signal, even if the remanence does not. First, Elmore and van der Voo (1982) maintained that the hematite remanence may in fact be a vector average of pre- and post-depositional hematite. Second, some hematite, as determined by Elmore and van der Voo (1982), is detrital and SP in size, which is too small a grain size to contribute to magnetic remanence; however, it will contribute to our susceptibility measurements. Third, although some martitization is believed to have occurred post-deposition, the abundance of martite matters more than when it altered, and variations in abundance are presumably related to depositional variations. This is because the martitization is an altered product of the detrital magnetite so any depositional cycles associated with the martite variation should remain, even after the transformation from magnetite to hematite. The martite more or less acts as a placeholder for the original magnetite. Similarly, any form of hematite that resulted from the replacement of a depositional mineral should retain the depositional signal. Only if entirely new hematite precipitates as the result of the transportation of ions into the matrix will the post-depositional hematite be of greater concern since it won't be reflective of a detrital signal. It is possible though that if new minerals are produced, their concentration may still reflect some aspect of the original depositional materials, such as porosity, which means that the original depositional signal could still be maintained. Fourth, the paleocurrent direction determined from the AMS fabric is consistent with the direction determined from bedding features (see *Sec. 4.5.2*). The anisotropy clearly reflects a depositional orientation. However, one could imagine a secondary, authigenic hematite forming around depositionally aligned minerals, resulting in a distribution anisotropy (Hargraves et al., 1991).

To examine in more detail the underlying physical variations that may be linked to susceptibility variations, the high-resolution susceptibility grids may be useful. Grid 1, although too small to capture the periodicity of variability observed in the stratigraphy, did demonstrate susceptibility variations associated with shifts in grain size. Lower medium grains, the coarser of the grain sizes present within this grid, and the foresets at the base of the grid, which represent a wider range of grain size variation than the rest of the grid, were both associated with higher susceptibility measurements. These areas of high susceptibility may have been influenced by an influx of different source materials during deposition that had greater abundance of magnetic minerals. Another explanation could be that the foresets at the base of the grid and the areas with larger grain sizes may have yielded greater interstitial space or secondary voids, possibly a result of well sorted grains, meaning low grain-to-grain contacts. Greater voids would have provided more space within which authigenic, box-work hematite could grow and latch on to the matrix minerals that cemented the sandstone together during diagenesis. Low susceptibility was observed within the middle of the grid between the top and bottom bounds of higher susceptibility, and was associated with fine-grained sandstone. The fine-grained sandstone likely represents less interstitial space meaning less secondary hematite could develop and thus presents with lower susceptibility measurements. This line of thought would suggest that susceptibility variability is representative of a secondary trait of deposition, such as porosity rather than a changing influx of depositional magnetic materials.

Grid 2 was again too small to capture the frequency of magnetic variability that was observed stratigraphically. However rather than demonstrating magnetic variability associated with grain size as was observed for Grid 1, high and low susceptibility measurements seem to associate with bed-forms, color changes, or erosional boundaries. Most of the lowest susceptibility measurements correlated well with erosional boundaries or color changes while high susceptibility measurements existed between these lows and were associated with large cross beds. The susceptibility highs within the cross beds were likely influenced by an influx of material that either brought greater abundance of magnetic materials or provided greater void space for accumulation of authigenic hematite. Meanwhile erosional boundaries potentially represent a shift to finer grain sizes of lower porosity as was represented by the measurements of low susceptibility. Transect 1, demonstrated a low susceptibility measurement at a slight color change boundary (upper left of Fig. 21) that seemed to be expressed in Transect 2 & 3 along the same, laterally extending, color shift contact (Fig. 21). The red bed color of the CHC has often been attributed to the fine-grained pigmentary hematite associated with either pre- or post-depositional clay rims. At this color boundary, the sandstone's pigment shifted from a deep red to a light, bleached red which may indicate a changing concentration of pigmentary hematite, from high to low. The color shift may be related to less dehydration of iron-bearing silicates within the dune feature that is formed in an arid environment, likely influenced by occasional overland floods. Since there is a lack of vegetation during the Precambrian, every rainfall event could produce overland flooding on an alluvial fan surface such as the setting for our locality. If such rainfall events were related to climate, they could potentially influence increased or decreased dehydration of the iron-bearing silicates present at the site.

Based on the observations made at the finer timescales captured by these grids, high and low susceptibilities seem to be closely related to bedding features and characteristics. Additionally, the general trend of successive, stratigraphic, susceptibility measurements saw an increase up-section. This may be explained by the source material changing due to variations in erosion patterns over time. Another interpretation is that dehydration weathering increased up-section due to intensifying subaerial weathering conditions of alluvial sediment. Increased weathering of the detrital material may have contributed to an increased presence of authigenic hematite that would also have recorded as higher susceptibility measurements.

If chronology was better established for the facies or if there was an estimated accumulation rate, we could determine a true periodicity for our successional susceptibility measurements, which would allow for a more complete spectral analysis. Unfortunately, the CHC formation occurs entirely within a normal magnetic polarity interval (Ojakangas et al., 2001). Without polarity boundaries or other clear indications of accumulation rates for our stratigraphic section, we are unable to conduct a full cyclostratigraphic analysis. Nevertheless, if we accept that our susceptibility data plausibly reflect climatically-influenced variations, we may begin to consider what the cycles might represent.

Our susceptibility spectral data output can be compared with Milankovitch cycles to assess the feasibility that the variations are orbitally-forced. The frequencies determined from the spectral output indicated a spectral peak of >99% confidence at 0.48 m^{-1} or every 2.08 m.

This frequency would represent accumulation rates for short eccentricity (100 kyr) at 0.021 mm/yr, long eccentricity (413 kyr) at 0.005 mm/yr, precession (26 kyr) at 0.080 mm/yr, and obliquity (41 kyr) at 0.051 mm/yr. Our peaks of lower confidence levels were also compared with the Milankovitch intervals, and these calculated accumulation rates were comparable to what was calculated for the >99% confidence peak. An example of a sedimentation rate averaged over the entire lake basin of the East African rift lake, Lake Tanganyika, was found to be approximately 0.477 mm/yr (Cohen et al., 1993). Whereas sediments of the Precambrian Belt Basin of the Northwestern United States fed into a sea and are estimated to have had a sedimentation rate of approximately 0.051 mm/yr (Harrison, 1972). Although the rates from this study (assuming orbital forcing) don't seem completely unreasonable when compared with the proposed Precambrian Belt Basin sedimentation rates, due to the uncertainty of the depositional timescale of our section it is impulsive to consider them as true sedimentation rates. Additionally, the CHC sediment accumulation was in a lacustrine setting, not a marine environment. Alternatively, it is possible that these measured frequencies are representative of shorter period climatic fluctuations of the Precambrian. Modern analogs for shorter climatic fluctuations that affect temperature, rainfall, and degree of humidity or aridity include the El Niño Southern Oscillation (ENSO), which occurs over brief intervals of approximately nine to twelve months at a time every three to seven years, on average (Malone et al., 2014). The Pacific Decadal Oscillation is similar to ENSO, but has the ability to persist for extended periods from 15-20 years or 50-70 years at a time (Mantua and Hare, 2002).

The CHC formation of Union Bay presented many complications, however we were able to distinguish some cyclicity from these Precambrian, fluvial red beds using outcrop based, magnetic susceptibility. To tease out the relationship that authigenic and detrital hematite shares with the depositional fabric, future work could emphasize detailed petrologic and provenance studies. To further determine if magnetic susceptibility measurements of fluvial red beds do indeed maintain frequencies related to astronomical cycles, a proposed study needs to target a section that has well established chronostratigraphy. For example, the Triassic-Jurassic Period saw the development of the Pangean basin between modern day North America and Africa (Olsen et al., 2003). The rift basin deposits from this time are exposed throughout much of the United States, Morocco, and parts of Canada (Olsen et al., 2003). The Bigoudine Formation in the Argana Basin of Morocco is one of these exposures (Olsen et al., 2003). It has been well dated thanks to its correlation with the Newark basin, of the United States, and the Newark basin's well established geomagnetic polarity timescale (Et-Touhami et al., 2008). While magnetocyclostratigraphic studies have been conducted on the Newark Basin (Olsen et al., 2003), such a study would benefit refinement of timescales within the Bigoudine Formation as well. Additionally, the certainty of geologic time for this unit along with a comparable study already developed from an adjacent portion of the same basin provides an excellent base from which to test for astronomically forced cycles maintained by deposition.

CHAPTER 6. CONCLUSIONS

Two magnetic components were found in the CHC at Union Bay: (titano-)magnetite and (titano-)hematite. The low coercivity, soft magnetic component likely represents fine-grained titanomagnetite to magnetite which accounts for the least dominant contribution to magnetic susceptibility. The high coercivity, hard magnetic component likely represents fine-grained hematite or titanohematite, which correlates strongly with magnetic susceptibility. It was demonstrated that these two components could be quantified using IRM un-mixing, IRM backfield, and χ(T). The bulk susceptibility correlates positively with the hard-magnetic component, suggesting that hematite contributes most strongly to outcrop magnetic susceptibility measurements. Specimens have a low degree of magnetic anisotropy, and the AMS fabric is primarily prolate and lineated. The AMS magnetic fabric suggests that a paleocurrent trending to the NW influenced the depositional orientation of the magnetic mineralogy at this site and was found to correspond well with prior studies that observed bedding features or clast imbrication to determine flow orientation. The correspondence between AMS fabric and paleocurrent measurements supports the interpretation that hematite orientation is representative of depositional conditions. Stratigraphic susceptibility increases up-section and following a spectral analysis, the data demonstrate several significant frequencies of variation, most prominently a 2.08 m cycle at >99% confidence. Since the depositional timescale of our section is uncertain, it is not possible to conclusively correlate the observed, significant periodicities with orbital forcing. Meanwhile, smaller-scale susceptibility grids represent a smaller overall range of magnetic susceptibility and demonstrate variations at spatial scales smaller than what was captured in the stratigraphic section. The highest susceptibility measurements taken at the outcrop are associated with large cross beds and relatively larger, physical grain sizes. The lowest susceptibility measurements correspond with erosional boundaries and small physical grain sizes. Whether or not susceptibility variations correlate with climate, they still likely relate to a variety of depositional properties of the sedimentary facies. Ultimately, this study concludes that magnetic characteristics of deep time, fluvial red beds can represent depositional variations. Therefore, these deposits are potential candidates that could be used to further constrain timescales of variation during the Precambrian provided absolute depositional timescales have been established for the unit in question.

REFERENCES

Bornhorst, T. J., & Barron, R. J. (2013). Geologic Overview of the Keweenaw Peninsula, Michigan. Institute on Lake Superior Geology Proceedings, 59th Annual Meeting, Houghton, MI, v. 59, part 1, 1-118.

Butler, R. F. (1992). *Paleomagnetism: Magnetic Domains to Geologic Terranes.* Tucson, Arizona, Department of Geosciences, University of Arizona: Blackwell Scientific Publications.

Cheel, R. (2002). Introduction to Clastic Sedimentology: Chapter 5. Bedforms and Stratification Under Unidirectional Flows. Ontario, Canada, Department of Earth Sciences, Brock University.

Cohen, A. S., Soreghan, M. J., & Scholz, C. A. (1993) Estimating the Age of Formation of Lakes: An Example from Lake Tanganyika, East African Rift System. *Geology, 21,* 511-514.

Dekkers, M. J. (2001). Rockmagnetism and Paleomagnetism. In *Encyclopedia of Life Support Systems*. (Vol. II, 1-3) Utrecht, Netherlands: Geophysics and Geochemistry.

DuBois, P. M. (1962). Paleomagnetism and Correlation of Keweenawan Rocks. Bulletin 71, *Geological Survey of Canada, Department of Mines and Technical Surveys*, Ottawa, Canada.

Egli, R. (2003). Analysis of the Field Dependence of Remanent Magnetization Curves. *Journal of Geophysical Research, 108(B2)*, 1-25.

Egli, R. (2004). Characterization of Individual Rock Magnetic Components by Analysis of Remanence Curves. 2. Fundamental Properties of Coercivity Distrubtions. *Physics and*

Chemistry of the Earth Parts A/B/C, 29, 851-867.

Elmore, R. D. (1981). The Copper Harbor Conglomerate and Nonesuch Shale, Sedimentation in a Precambrian Intracontinental Rift, Upper Michigan*.* *PhD dissertation*, University of Michigan, Ann Arbor, Michigan.

Elmore, R. D. (1984). The Copper Harbor Conglomerate: A Late Precambrian Fining-Upward Alluvial Fan Sequence in Northern Michigan. *Geological Society of America Bulletin, 95*, 610-617.

Elmore, R. D., & van der Voo, R. (1982). Origin of Hematite and its Associated Remanence in the Copper Harbor Conglomerate (Keweenawan), Upper Michigan. *Journal of Geophysical Research, 87(B13)*, 918-928.

Et-Touhami, M., Olsen, P. E., Kent, D. V., Fowell, S. J., & Whiteside, J. H. (2008) Tectonostratigraphy, Biostratigraphy, and Magnetostratigraphy of Late Triassic-Early Jurassic Red Beds in Morocco: An Overview, Abstract 90074, presented at 2007 First Morocco Association of Petroleum Goelogists International Convention, Conference & Exhibition, Marrakech, Morocco, 28-31, Oct.

Flinn, D. (1982). On Folding During Three-Dimensional Progressive Deformation. *Geological Society of London Quarterly Journal, 118*, 385-433.

Gordon, M. B., & Hempton, M. R. (1986). Collision-Induced Rifting: The Grenville Orogeny and the Keweenawan Rift of North America. *Tectonophysics, 127*, 1-25.

Green, J. C. (1982). Geology of Keweenawan Extrusive Rocks. *Geological Society of America, 156*, 47-55.

Hargraves, R. B., Johnson, D., and Chan, C. Y. (1991). Distribution Anisotropy: The Cause of AMS in Igneous Rocks? *Geophysical Research Letters, 18*, 2193-2196.

Harrison, J. E. (1972). Precambrian Belt Basin of Northwestern United States: Its Geometry, Sedimentation, and Copper Occurrences. *Geological Society of America Bulletin, 83*, 1215-1240.

Hays, J. D., Imbrie, J., & Shackleton, N. J. (1976). Variations in the Earth's Orbit: Pacemaker of the Ice Ages. *Science, 194(4270)*, 1121-1132.

Heslop, D. (2015). Numerical Strategies for Magnetic Mineral Un-Mixing. *Earth-Science Review, 150*, 256-284.

Heslop, D., & Dillion, M. (2007). Unmixing Magnetic Remanence Curves without a Prior Knowledge. *Geophysics Journal International, 170*, 556-566.

Heslop, D., Dekkers, M. J., Kruiver, P. P., & van Oorschot, I. H. (2002). Analysis of Isothermal Remanent Magnetization Acquisition Curves Using the Expectation-Maximization Algorithm. *Geophysical Journal International, 148(1)*, 58-64.

Hnat, J. S., van der Pluijm, B. A., & van der Voo, R. (2006). Primary Curvature in the Mid-Continent Rift: Paleomagnetism of the Portage Lake Volcanics (Northern Michigan, USA). *Tectonophysics, 425*, 71-82.

Kodama, K.P. (2016). Rock Magnetic Cyclostratigraphy of the Mississippian Mauch Chunk fm. Pottsville, Pennsylvania, Abstract GP51D-05, presented at 2016 AGU Fall Meeting, San Francisco CA, 12-16, Dec.

Kodama, K. P., & Hinnov, L. A. (2015). *Rock Magnetic Cyclostratigraphy*. Chichster West Sussex, England: John Wiley & Sons.

Kodama, K. P., Anastasio, D. J., Newton, M. L., Pares, J. M., & Hinnov, L. A. (2010). High-Resolution Rock Magnetic Cyclostratigraphy in an Eocene Flysch, Spanish Pyrenees. *Geochemistry, Geophysics, Geosystems, 11*, 1-22.

Kruiver, P. P., Dekkers, M. J., & Heslop, D. (2001). Quantification of Magnetic Coercivity Components by the Analysis of Acquisition Curves of Isothermal Remanent Magnetization. *Earth and Planetary Science Letters, 189*, 269-276.

Kulakov, E. V., Smirnov, A. V., & Diehl, J. F. (2013). Paleomagnetism of ~1.09 Ga Lake Shore Traps (Keweenaw Peninsula, Michigan): New Results and Implications. *Canadian Journal of Earth Science, 50*, 1085-1096.

Langford, R. P., & Chan, M. A. (1989). Fluvial-Aeolian Interactions: Part II, Ancient Systems. *Sedimentology, 36*, 1037-1051.

Liu, Q., Roberts, P. A., Larrasoana, J. C., Banerjee, S. K., Guyodo, Y., Tauxe, L., & Oldfield, F. (2012). Environmental Magnetism: Principles and Applications. *Reviews of Geophysics, 50* (RG4002), 1-50.

Malone, S. L., Staudhammer, C. L., Oberbauer, S. F., Olivas, P., Ryan, M. G., Schedlbauer, J. L., Loescher, H. W., Starr, G. (2014). El Niño Southern Oscillation (ENSO) Enhances CO_2 Exchange Rates in Freshwater Marsh Ecosystems in the Florida Everglades. *PLOS ONE 9(12)*, 1-30.

Mantua, N. J. & Hare R. S. (2002). The Pacific Decadal Oscillation. *Journal of Oceanography,* 58, 35-44.

Maxbauer, D. P., Feinberg, J. M., & Fox, D. L. (2016). MAX UnMix: A Web Application for Un-mixing Magnetic Coercivity Distributions. *Computers and Geosciences, 95*, 140-145.

Michigan Department of Natural Resources. (n.d.) Geologic Map Porcupine Mountains Wilderness State Park. *Michigan DNR*, 2. Retrieved from https://www.michigan.gov/documents/dnr/PMGEO_446415_7.pdf.

Moorhouse, B. L., and White, J. D. L. (2016). Interpreting Ambiguous Bedforms to Distinguish

Subaerial Base Surge from Subaqueous Density Current Deposits. *The Depositional Record, 2(2)*, 173-195.

Moskowitz, B. M. (1991). *Hitchhiker's Guide to Rock Magnetism: Classes of Magnetic Minerals*. Retrieved September 2017, from Institute of Rock Magnetism, Univeristy of Minnesota: http://www.irm.umn.edu/hg2m/hg2m_b/hg2m_b.html.

Mountney, N. P. (2006). Eolian Facies Models, Facies Models Revisited. *SEPM Society for Sedimentary Geology Special Publication, 84*, 19-83.

Noffke, N. (2009). The Criteria for the Biogeneicity of Microbially Induced Sedimentary Structures (MISS) in Archean and Younger, Sandy Deposits. *Earth-Science Reviews, 96*, 173-180.

Ojakangas, R. W., Morey, G. B., & Green, J. C. (2001). The Mesoproterozoic Midcontinent Rift System Lake Superior Region, USA. *Sedimentary Geology* (141-142), 421-442.

Olsen, P. E., Kent, D. V., Et-Touhami, M., & Puffer, J. (2003) Cyclo-, Magneto-, and Bio-Stratigraphic Constratins on the Duration of the CAMP Event and its Relationship to the Triassic-Jurassic Boundary. *The Central Atalantic Magmatic Province: Insights from Fragments of Pangea, 136*, 7-32.

Olsen, P. E., Kent, D. V., Cornet, B., Witte, W. K., & Schlische, R. W. (1996). High-Resolution Stratigraphy of the Newark Rift Basin (early Mesozoic, Eastern North American). *Geological Society of America Bulletin, 108(1)*, 40-77.

Robertson, D. J., & France, D. E. (1994). Discrimination of Remanence-Carrying Minerals in Mixtures Using Isothermal Remanent Magnetization Acquisition Curves. *Physics of the Earth Planetary Interiors, (82)*, 223-234.

Stein, C. A., Kley, J., Stein, S., Hindle, D., & Keller, G. R. (2015). North America's

Midcontinent Rift: When Rift met LIP. *Geosphere, 11(5)*, 1607-1616.

Stein, C. A., Stein, S., Merino, M., Keller, G. R., Flesch, L. M., & Jurdy, D. M. (2014). Was the Mid-Continent Rift Part of a Successful Seafloor-Spreading Episode? *Geophysical Research Letters, 41(5)*, 1-14.

Stein, Seth, Carol Stein, Jonas Kley, Randy Keller, Miguel Merino, Emily Wolin, Douglas Wiens, Michael E. Wyession, Ghassan Al-Equabi, Weison Shen, Andrew Frederiksen, Fiona Darbyshire, Donna Jurdy, Greg Waite, William Rose, Wrika Vye, Tyrone Rooney, Robert Moucha, and Eric Brown. (2016). New Insights into North America's Midcontinent Rift. *EOS, 97*, 1-14, https://doi.org/10.1029/2016EO056659.

Stockhausen, H. (1998). Some New Aspects for the Modelling of Isothermal Remanent Magnetization Acquisition Curves by Cumulative log Gaussian Functions. *Geophysical Reserarch Letters (25)*, 2217-2220.

Tauxe, L. (2016). Chapter 13: Paleomagnetic Tensors. In L. Tauxe, *Essentials of Paleomagnetism* (3rd Web Edition ed.). EarthRef.org.

Taylor, I. E., & Middleton, G. V. (1990). Aeolian Sandstones in the Copper Harbor Formation, Late Proterozoic, Lake Superior Basin. *Canadian Journal of Earth Sciences, 27(10)*, 1339-1347.

Tohver, E. W., van der Pluijm, B., Geraldes, M. C., Bettencourt, J. S., & Rizzotto, G. (2006). Restored Transect Across the Exhumed Grenville Orogen of Laurentia and Amazonia with Implications for Crustal Architecture. *Geological Society of America, Geology, 34(8)*, 669-672.

United States Geological Survey, Daniels, D.L., & Snyder, S. L. (n.d.). Shaded-Relief Total

Magnetic Intensity Anomaly Map. Total Field Aeromagnetic Anomaly Map. *University of Minnesota.* Retrieved from www.mngs.umn.edu/nicegeo/pdfs/shd_tfmag.pdf.

Vincenz, S. A. (1968). Phenomenon of Partial Self-Reversal in Keweenawan Rocks: 1. Magnetization of Portage Lake Lavas. *Journal of Geophysical Research, 73*(8), 2729-2752.

Vrazo, M. B., Benton, M. J., Daeschler, E. B. (2007). Tetrapod tracks from the Mauch Chunk Formation (middle to upper Mississippian) of Pennsylvania, U.S.A. *The Academy of Natural Sciences of Philadelphia, 156(1)*, 199-209.

Wilmeth, D. T., Dornbos, S. Q., Isbell, J. L., & Czaja, A. D. (2014). Putative Domal Microbial Stuctures in Fluvial Silicicalstic Facies of the Mesoproterozoic (1.09 Ga) Copper Harbor Conglomerate, Upper Peninsula of Michigan. *Geobiology (12)*, 99-108.

Wolff, R. G., & Huber, N. K. (1973). The Copper Harbor Conglomerate (Middle Keweenawan) on Isle Royale, Michigan, and its Regional Implications. Geological Survey Professional Paper 754-B, United States Department of the Interior. Washington D.C.: Geological Survey.

APPENDIX:

Empty Tube Data Used for Furnace Correction

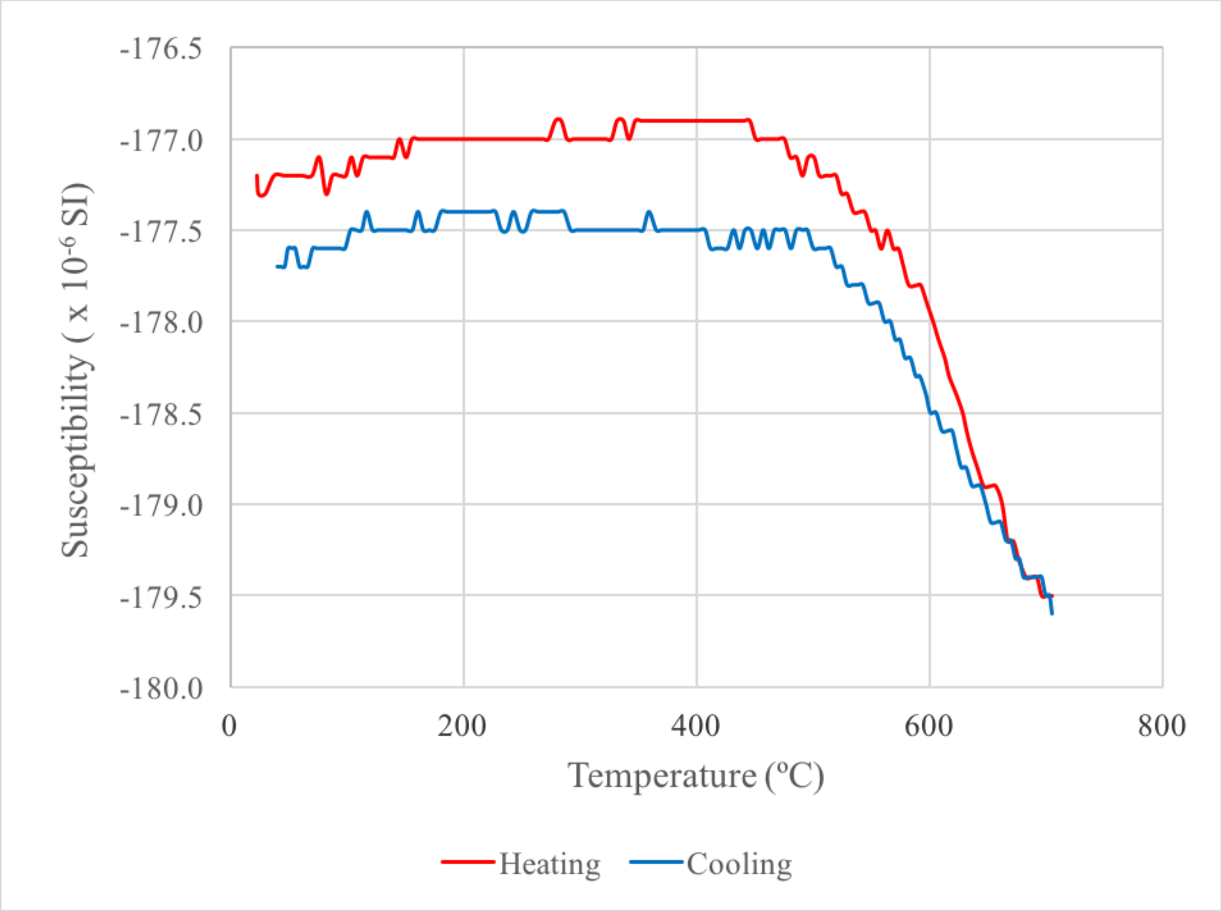

Figure 23: Empty tube used to measure χ(T) in furnace attachment of Kappabridge

The magnetic susceptibility of the blank tube that was used to measure the furnace correction for magnetic susceptibility of CH16 χ(T).